Deformation and strain localization in polycrystals with plastically heterogeneous grains

M. Khadyko[1], C. D. Marioara[2], I. G. Ringdalen[2], S. Dumoulin[2] and O.S. Hopperstad[1].

[1] *Structural Impact Laboratory (SIMLab), Centre for Research-based Innovation, Department of Structural Engineering, Norwegian University of Science and Technology, NO-7491 Trondheim, Norway*

[2]*SINTEF Materials & Chemistry, NO-7465 Trondheim, Norway*

Abstract

A model of a polycrystalline material is studied, where each grain consists of several zones with different plastic properties. The size and configuration of the zones as well as their properties are mimicking the situation inside the crystals of artificially aged Al alloys with precipitate free zones (PFZs). The properties of the different zones are conjectured based on micromechanical models and experimental observations of the AA6000 series of Al alloys. A periodic patch of such a composite material, subjected to plane-strain tension, is modelled using the finite element method. The material behaviour is described by a single crystal plasticity model. The results of the simulations show a number of characteristic features emerging in composite material systems, including sliding and distortion of grain boundaries and shear band formation at grain boundary triple points. The assumptions made about the properties of the different zones in the crystals are evaluated. The distributions of plastic strain and deviatoric and hydrostatic stresses in the composite crystalline systems are discussed.

1. Introduction

Metallic materials are usually treated as homogeneous in practical applications, and criteria for yielding, strain localization and fracture are formulated in terms of mechanical fields acting on a homogeneous material subjected to certain boundary conditions. Any details of the microstructure are not considered explicitly and the material properties are derived from the results of macroscopic mechanical tests and some basic assumptions about the material behaviour (e.g. yielding, work-hardening and rate sensitivity). This approach produces useful results, but its scope is limited. If the knowledge about the material comes only from macroscopic mechanical tests, predictions of the material behaviour outside the domain of these tests will be just extrapolations. The accuracy of these extrapolations will depend on the accuracy of the basic assumptions. On the other hand, if a connection can be established between the material's microstructure and its macroscopic properties, more accurate predictions can be made, relying more on the underlying physical mechanisms than on mechanical tests and assumptions. The problem with this approach lies in the complexity and variety of the microstructural features encountered in real materials at small scales. An Al alloy is an aggregate of crystalline grains with different orientations and morphologies divided by grain boundaries. Inside the grains the material includes particles of various composition, strength, shape and size. The interfaces between all the constituent parts are an important class of microstructural features with complex behaviour as well. The lattice of the crystal includes defects, such as dislocations and their substructures (e.g. dislocation cells and dislocation pile-ups) and vacancies. If a model aims to accurately predict the properties of such a material, it should include enough of these features to be representative and at the same time be detailed and precise in their description — this is usually not possible in practice; neither analytically nor numerically.

Nevertheless, in some cases, a microstructural feature may be so prominent and important that even including some simplified representation of it in the material model may already markedly improve the model's prediction accuracy and reduce the reliance on mechanical testing. One example of such a microstructural feature could be the crystallographic texture that plays a central role in defining the plastic anisotropy of a polycrystalline material. If the crystallographic texture is measured and represented by a statistical set of orientations, the plastic anisotropy of the material may be predicted using this set in a crystal plasticity framework [1-7].

Another example is the Kocks-Mecking model of work-hardening. It is based on the analysis performed by Taylor [8] on a simplified dislocation structure, which resulted in an equation that connects the dislocation density and the global shear stress necessary to start the dislocation movement (i.e., to produce plastic strain). Kocks and Mecking added a rule for the dislocation density evolution in [9, 10] and proposed a model that predicts the work-hardening rate of a material even if one considers the dislocation cell structures [11, 12]. The physical nature of the model combined with its simplicity and possibilities for modifications made it very broadly used. The works that modify and enhance the basic model include [13-20]. The problems studied with versions of Kocks-Mecking model include the influence of grain size and grain boundaries on the properties of the polycrystals [21-23], changing loading paths and latent hardening [24-26], thin film deformation [27, 28], void growth and interaction [29, 30] and multiphase alloys [31].

One more example of a crucial microstructural feature that may define a macroscopic property in a certain way is the precipitate particles that form in age-hardening Al alloys after heat treatment. The most important role of these particles in the alloy is to serve as additional dislocation obstacles, trapping mobile dislocations and thus increasing the yield stress. If the particles are non-shearable, geometrically necessary dislocations will accumulated around them and contribute to an increase of the work-hardening rate. Ashby used a simplified model to analyse the generation of geometrically necessary dislocations around non-shearable particles in [32, 33]. His results were used in [34] to estimate the stress-strain curve of the AA6000 series Al alloys with an arbitrary heat treatment.

In other cases the connection between a microstructural feature and the macroscopic behaviour is not as explicit or strong as in these examples. Nevertheless the understanding of the mechanisms operating at microlevel is necessary to improve higher level models. An example of this type of study may be found in [35-37]. The inhomogeneous deformation in a crystal consisting of several different phases is studied based on a laminate model, with varying thickness and strength of the layers. Strain gradient plasticity is used to reveal the influence of the characteristic lengths and interface conditions on the global response of the laminate and the local mechanical fields. The simplicity of the laminate model allows the use of advanced material models and sometimes an analytical solution. While this laminate does not correspond directly to any physical system, the obtained results may be (with some reservations) extended to the behaviour of precipitate particles, multiphase crystals or thin films.

Other works which utilize simplified models to study complex systems include [38], where the precipitates in the heat-treated crystal are modelled as a periodic cubic array of spherical particles. The crystal is also simplified to a single slip plane, so that an advanced strain gradient plasticity model could be used to study the dislocation density distribution around the particles. In [39] shearing of a thin crystalline strip is studied, and in [40] a soft plastic channel in a harder medium is used to represent phenomena like slip bands in crystals.

One of the prominent microstructural features, which may be found in heat-treated alloys, is the precipitate free zones (PFZs) which form on the grain boundary. During the heat treatment the grain boundary acts as a sink for solute atoms and vacancies. This leads to formation of large precipitates on the grain boundary and an adjacent zone depleted of alloying elements and vacancies. The relative purity of the material in the PFZs, i.e., lack of dislocation obstacles, leads inevitably to the assumption that this zone is softer than the rest of the crystal, which is reinforced with solute atoms of the alloying elements and precipitate particles. Nano-indentation tests [41] confirm this hypothesis. On the other hand, one can assume that under straining dislocations will accumulate in the PFZs and work-harden these zones in the same way as any other crystal. The influence of the PFZs on the deformation and fracture of polycrystals has been studied by use of simplified models. In [42] crystals with PFZs are represented by a regular hexahedral structure. The width of the real PFZs may be from 100 to 10000 times smaller than the grain diameter. This makes a direct one-to-one modelling, e.g. with the finite element method (FEM), very complex, so in [42] the PFZs are much wider relative to the grain diameter. The material in the PFZs is modelled with porous plasticity, following the aforementioned assumptions about its lower yield stress and high work-hardening rate. The same regular hexagonal grain geometry and broad PFZs, but with a more advanced material model, was used in [43, 44]. The influence of grain shape on the behaviour of such a system was studied, among others, in [45]. The softer PFZ may be assumed to deform differently than the rest of the grain, thus producing considerable plastic strain gradients from early stages of deformation. The strain gradient plasticity model was applied to the same hexagonal grain model type in [46]. The results showed that in that case the strain gradient hardening will very quickly make the PFZ stronger than the rest of the grain and prevent further plastic deformation in the PFZ.

An experimental study of PFZs in a material under deformation could answer many questions, but this is a complicated task. PFZs in the undeformed and deformed states were studied with electron microscopy since [47] and [48], but even these two studies came to

somewhat opposite conclusions about the deformation mechanisms in a crystal with PFZs. Later, when the importance of PFZs for the fracture initiation and propagation was recognized, the behaviour of PFZs with respect to ductile fracture became the focus of the studies [49-53]. These studies mostly address the late stages of deformation, particle decohesion, and void nucleation, growth and coalescence. Being the softest part of the grain, PFZs are the location of intergranular fracture initiation, which separates the grains but leaves them otherwise intact. Quite often a competition between intergranular and intragranular fracture is observed, where the latter implies that fracture takes place inside the grains themselves, instead of in the PFZs. Some attempts have been made to predict the fracture mode from the loading conditions and the constituent properties of the grains and the PFZs, see [43-45, 54, 55]. Yet the mechanical behaviour of the crystals in and around the PFZs remains in many ways in the realm of speculation. In [56] and [49] large plastic deformation is observed in the PFZs before fracture initiation. Such deformation would normally lead to immense accumulation of dislocations, but in some cases this was not observed[47, 53]. Instead dislocation pile-ups were only found in the transition zone between the PFZ and the interior of the grain. Some direct observations of the dislocation movement in the PFZs at the early stages of deformation were made in [57], which showed that the dislocations in the PFZ tend to move away from the grain boundary and accumulate just outside the PFZ. This kind of behaviour may be compared to the behaviour of a dislocation channel subjected to constrained shearing, a configuration sometimes used to test analytical and numerical dislocation dynamics models [58-60].

In the present work the primary interest lies in the mechanical fields in a polycrystal containing hard grains divided by soft layers. The emphasis is on the plastic deformation and localisation processes and their possible connection to the fracture regime. Compared to real Al alloys with PFZs, the soft zones in the considered crystalline composite are very wide. The finer details of the dislocation dynamics and the dislocation-induced hardening are simplified and a phenomenological approach is used to model the material properties. Therefore, one should be cautious when interpreting the results, which can be applied to real materials only with some reservations. On the other hand, the high strength-low hardening Al alloys, in which the PFZs are found, are prone to strain localisation, like shear banding, which most of the PFZ models ignore. The modelling of strain localisation in crystalline materials using the FEM is a well-developed field [61-64], yet it has, to the authors' best knowledge, never been applied in the context of PFZ studies. The crystalline composite model and the material

properties of the constituent zones were conjectured based on the results of a TEM study, presented in Section 2. An AA6060 alloy was heat treated to the T6 temper and used to produce uniaxial tensile specimens. TEM specimens were cut from different parts of the deformed tensile specimens, so that the studied material was subjected to strains ranging from 0% (undeformed material) to 120% (near the fracture surface). The most notable result of the study was that the dislocation structures, characteristic for the forest hardening, were observed neither for moderately deformed PFZ nor for the extremely deformed ones. The dislocations that nucleated in the PFZ and carried the plastic deformation through them tended instead to accumulate in pile-ups in the grain interior. Therefore, the PFZ was assumed to deform without work-hardening in the crystal composite model, and an additional pile-up layer of material with very high hardening capacity was added between the PFZ and the grain interior. The grain interior was modelled in a more traditional way, using the Kocks-Mecking work-hardening model [10] as it was formulated in [65].

2. Experimental study

Material and methods

An AA6060 Al alloy was extruded into a 10 mm thick and 90 mm wide flat profile. The chemical composition of the alloy is given in Table 1. The profile has a typical recrystallized grain structure, consisting of grains, moderately elongated along the extrusion direction, with average diameter of 60 μm and aspect ratio of 1.5. The grain structure is presented in Figure 1. The alloy has a strong cube texture with a minor Goss component. Cylindrical specimens for tensile testing with 10 mm diameter and 40 mm gauge length were machined from the profile in the transverse direction. The specimens were heat-treated to T6 temper. Quasi-static tension tests were conducted at room temperature until fracture. A comprehensive description of the material, test procedures and results is given in [4].

Transmission Electron Microscopy (TEM) specimens were prepared from transverse discs of a fractured tensile test sample such that the observation direction was along the tensile direction (i.e., the transverse direction of the extruded profile). Transverse discs of about 1 mm thickness were taken from three locations of the tensile test sample, see Figure 2: the undeformed grip area (section A), the gauge area outside the diffuse neck (section B), and close to the fracture surface inside the neck (section C). The strain in the gauge area outside the diffuse neck is about equal to the uniform strain of the alloy, namely 9%, while the strain

inside the neck and close to the fracture surface is much higher. The fracture strain of the AA6060 alloy in temper T6 is about 120% [4]. In addition, normal discs were extracted inside the neck and even closer to the fracture surface with observation direction in the thickness (or normal) direction of the extruded profile (section D). The transverse and normal discs were ground to foils 80 to 100 μm thick using rotating SiC abrasive papers of different fineness, and from these foils 3 mm diameter TEM specimens were punched. The TEM specimens were electro-polished using a Tenupol 3 instrument. The electrolyte consisted of $1/3^{rd}$ HNO_3 in methanol, and the solution was kept at temperatures from -20°C to -35°C.

A Philips CM30T TEM operated at 150 kV was used for recording diffraction contrast bright field images, used to visualise bulk precipitates, grain boundaries (GBs) and PFZs.

Results

The image in Figure 3 is obtained from the undeformed material inside the grip area of the tensile test sample (section A). The material shows a typical bulk microstructure, characterised by a homogeneous distribution of needle-shaped precipitates with lengths along <100>Al directions, which usually forms in the 6xxx Al-Mg-Si system. Figure 4 shows two examples of GBs and the corresponding PFZs. It can be observed that the low-angle GB (LAGB), see Figure 4 a), has a finer GB precipitation than the high-angle GB (HAGB), see Figure 4 b). In the LAGB case the adjacent grains share a common <001>Al direction at the GB, and formation of Mg-Si needle precipitates are favoured along this direction. From Figure 4 and similar images the extent of the PFZ, including the zones in the two adjacent grains, was estimated at approximately 200 nm.

The images in Figure 5 are obtained in the gauge area outside the diffuse neck (section B). The dislocations are clearly visible, interacting with the needle precipitates and being trapped by them. The dislocation density inside the grain is not uniform, with some areas displaying higher density than the others. Figure 6 shows TEM images recorded at GBs. The PFZs contain fewer dislocations than the interior of the grain. Furthermore, most of the dislocations that penetrate into the PFZs are in projection aligned perpendicular to the GBs, regardless the crystallographic orientation of the adjacent grains. These images may be compared with the image of the un-deformed material in Figure 4.

The dislocation distribution in the grain interior and around the GBs in the material inside the neck close to the fracture surface (section C) is similar to that of the material in the

gauge area outside the neck, see Figure 7 a). However, sometimes dislocation pile-ups were found close to and along the boundary between the grain interior and the PFZ, as indicated by the red arrow in Figure 7 b). In this case the amount of dislocations in the PFZ (which are perpendicular to the GB) is lower. Extreme cases were observed where the dislocation pile-up close to and along the interface between the grain interior and the PFZ is so dense that the whole PFZ area (including the GB in the middle) seems to be completely separated from the adjacent grains, becoming a band-like elongated grain on its own. One such example is shown in Figure 8 in which both images are taken from different parts of the same GB. The different diffraction contrast between the grain interior and the PFZ indicates slightly different crystallographic orientations and therefore the PFZ may be considered as a new band-like subgrain. It should be noted that this type of structure is an extreme case and was only found for the material inside the neck and close to the fracture surface, where it was encountered much less frequently than the structures of the type presented in Figure 8: a). The width of the band-like structures is larger (400 to 500 nm) than the measured width of the PFZ (approximately 200 nm). Therefore the dislocations in this case pile up close to the interface between grain interior and PFZ, but they are still part of the grain interior.

All the results above were obtained from observations along the tensile direction. Figure 9 shows a TEM image with observation direction along the normal direction of the extruded profile. This image is from within the neck area close to the fracture surface (section D). The aim was to find the angle between the tensile direction and the direction of GBs that display similar band-like structures as exemplified in Figure 8: b). The GB shown in Figure 9 exhibits this band-like structure and its angle with the tensile direction was measured to be approximately 40°. Another band-like GB was found in this TEM specimen and its angle with the elongation direction was approximately 30°.

3.   Microstructure of model material

The microstructure of a crystal, which consists of several zones with different plastic properties, and the parameters of the material model for these zones were conjectured based on the results of the TEM study described in the previous section.

The model material consists of periodic structures made of crystalline grains separated by border layers, as shown in Figure 10 a) and b). Figure 10 a) shows an approximately equiaxed structure consisting of 18 grains with random shape, typical for recrystallized Al

alloys, and Figure 10 b) displays a fibrous structure with 5 long grains (fibres) broken into subgrains by a low-angle boundary, typical for extruded Al alloys. The system was 2D with an imposed plane-strain condition, i.e., zero strain in the y-direction. Each grain was divided into three zones, as shown in more detail in Figure 11. The zones belonging to the same grain had different material properties but the same crystallographic orientation. Random crystallographic orientations were assigned to the grains of the recrystallized microstructure. For the fibrous microstructure, each fibre was assigned a random main orientation. The orientations of the subgrains of the fibres were rotated by 5° around all three axes, away from the main fibre orientation. The orientations of the neighbouring subgrains were rotated in the directions opposite to each other. Thus the misorientation between two neighbouring subgrains is always 10°, and the average of the subgrain orientations is equal to the chosen main orientation of the fibre. On the top and bottom edges of the fibrous microstructure a more simple grain with just two subgrains was used to reduce the number of edge nodes and the computation time.

The largest zone was the bulk of the grain. It represented a typical artificially aged Al alloy, containing precipitate particles that define its high yield strength and relatively low hardening capacity. The material model of this zone had one constant characteristic length associated with it, which was proportional to the average distance between the non-shearable precipitates. As the results of TEM confirm, the two main hardening mechanisms in this zone are the forest hardening and the non-shearable precipitate induced hardening. The dislocations get trapped on the particles and accumulate around them, until further dislocation accumulation is prevented by shearing of the particle by the produced stresses, particle decohesion or some other process. The material model used for the bulk of the grain followed closely the approach developed in [34]. Usually in crystal plasticity simulations this is the only zone that is included in the polycrystal model. For comparison, more traditional systems, shown in Figure 12, were also tested. They had exactly the same morphology and crystallographic orientations as the systems in Figure 10, but with grains modelled as homogeneous bulk zones and these are further referred to as the homogeneous models (in contrast to the model with different zones which is referred to as the composite models).

The two narrow zones at the borders of the grains represented the pile-up zone and the PFZ. Their modelling was based on the observations from [56, 57] and the dislocation dynamics modelling results from [58], as well as the study presented in Section 2. At the onset of plastic deformation the PFZ starts deforming first as the softest zone in the grain. The

dislocations move through it with little resistance and exit to the grain interior, as shown in [57]. There they are trapped by the precipitate particles. The addition of the growing plastic strain mismatch between the interior of the grain and the PFZ leads to creation of the pile-up zones just outside the PFZ. Eventually the pile-ups accumulate enough internal energy to facilitate some sort of qualitative change in the deformation by breaking the PFZ into the subgrains or leading to decohesion of grain boundary precipitate. In this work only the initial part of the deformation process was described, before such qualitative change.

The pile-up zone was assigned a characteristic length, which described the trapping of dislocations caused by the mismatch of the material properties and plastic deformation between the grain interior and the PFZ. The PFZ has no precipitate particles contributing to yield strength and work-hardening and the work-hardening mechanisms relevant for the PFZ are still unclear. The experimental observations in [49, 56] show that PFZs are capable of very high levels of plastic strain without reaching the strength of the grain interior, although the dislocation structures associated with forest hardening are not observed in them, as shown in Section 2 and in [53]. Hence, direct application of the strain gradient plasticity may greatly overestimate their strength [46]. Therefore in this study it was chosen to try to replicate the main features of these observations and the PFZs were modelled as dislocation channels with almost no work-hardening and no accumulation of dislocations in them. No special measures were taken to model the grain boundary or the grain boundary precipitates. In the present model the grain boundaries were just the transition lines between the zones with different crystallographic orientations. Some important mechanisms acting in the PFZs might have been ignored by the modelling approach adopted here. The pile-up zones could produce long-range stress fields which may contribute to work-hardening in the PFZs according to [58, 60]. The deformation in the PFZs may be a combination of the plastic deformation of the material and grain boundary sliding.

In addition to the speculative nature of the utilized modelling approach, one must keep in mind that the experimental data was obtained for uniaxial tensile tests with almost equiaxed 3D grains, while the numerical model is 2D and with an imposed plane-strain condition. The main trends of the plastic deformation in our composite material should be defined by the contrasting material properties of the grain interior, PFZ and pile-up zones, whatever the loading case. Nevertheless, the quantitative details may depend on the loading, e.g. strain localisation in form of shear bands develops much easier and earlier in the course of plastic deformation in the 2D plane strain model than in a 3D case, due to more constrained plastic

flow in the latter. Therefore the results of the simulations are not comparable to the experimental data in a quantitative manner. Nevertheless, the general characteristics of plastic deformation in a crystal with soft and hard zones should be reproduced by the present modelling approach, which was the goal of this work.

4. Constitutive modelling

The finite deformation formulation of single crystal plasticity is used. The deformation gradient $\boldsymbol{F}$ is multiplicatively decomposed [66] into an elastic part $\boldsymbol{F}^e$ and a plastic part $\boldsymbol{F}^p$ as

$$\boldsymbol{F} = \boldsymbol{F}^e \boldsymbol{F}^p \tag{1}$$

Here $\boldsymbol{F}^p$ accounts for plastic slip and transforms the crystal from the initial configuration Ω_0 into the intermediate plastically deformed configuration $\bar{\Omega}$, while $\boldsymbol{F}^e$ accounts for the elastic deformations and rigid body rotations and transforms the crystal from the intermediate configuration $\bar{\Omega}$ into the current configuration Ω. The following relations are formulated as in [67]. The slip systems are defined by the slip direction vector $\boldsymbol{m}_0^\alpha$ and the slip plane normal vector $\boldsymbol{n}_0^\alpha$ in the initial configuration. They stay the same in the intermediate configuration and transform into vectors $\boldsymbol{m}^\alpha$ and $\boldsymbol{n}^\alpha$, respectively, in the current configuration. These vectors may be used as a basis of the plastic velocity gradient $\bar{\boldsymbol{L}}^p$ in the intermediate configuration

$$\bar{\boldsymbol{L}}^p = \dot{\boldsymbol{F}}^p \left(\boldsymbol{F}^p \right)^{-1} = \sum_{\alpha=1}^{n} \dot{\gamma}^\alpha \boldsymbol{m}_0^\alpha \otimes \boldsymbol{n}_0^\alpha \tag{2}$$

where $\dot{\gamma}^\alpha$ is the slip rate on slip system α in the intermediate configuration and n is the total number of slip systems.

The elastic Green strain tensor $\bar{\boldsymbol{E}}^e$ with respect to the intermediate configuration may be defined as

$$\bar{\boldsymbol{E}}^e = \frac{1}{2}\left[\left(\boldsymbol{F}^e \right)^T \boldsymbol{F}^e - \boldsymbol{I} \right] = \frac{1}{2}\left(\bar{\boldsymbol{C}}^e - \boldsymbol{I} \right), \quad \bar{\boldsymbol{C}}^e = \left(\boldsymbol{F}^e \right)^T \boldsymbol{F}^e \tag{3}$$

where $\overline{C}^e$ is the elastic right Cauchy-Green deformation tensor and I is the second-order unity tensor. If the Cauchy stress tensor σ is pulled back into the intermediate configuration, the second Piola-Kirchhoff stress tensor $\overline{S}$ is obtained

$$\overline{S} = \det F \left(F^e \right)^{-1} \sigma \left(F^e \right)^{-T}$$
(4)

By assuming small elastic deformations, it is reasonable to adopt a linear hyperelastic model to describe the elastic behaviour

$$\overline{S} = \mathbf{C}_{el}^{\overline{S}} : \overline{E}^e$$
(5)

where $\mathbf{C}_{el}^{\overline{S}}$ is the fourth-order tensor of elastic moduli.

The total power per unit volume $\dot{w}$ consists of elastic and plastic parts

$$\dot{w} = \dot{w}^e + \dot{w}^p = \overline{S} : \dot{\overline{E}}^e + \overline{C}^e \overline{S} : \overline{L}^p$$
(6)

The plastic power may be rewritten as a sum of powers spent on all the slip systems

$$\dot{w}^p = \sum_{\alpha=1}^{n} \tau^{\alpha} \dot{\gamma}^{\alpha}$$
(7)

where τ^{α} is the resolved shear stress on slip system α, power conjugate to the slip rate $\dot{\gamma}^{\alpha}$, and may be found from the second Piola-Kirchhoff stress tensor as

$$\tau^{\alpha} = \overline{C}^e \overline{S} : \left(m_0^{\alpha} \otimes n_0^{\alpha} \right)$$
(8)

Flow and work-hardening rules

The plastic flow is described by a rate-dependent rule [68]

$$\dot{\gamma}^{\alpha} = \dot{\gamma}_0 \left(\frac{\left| \tau^{\alpha} \right|}{\tau_c^{\alpha}} \right)^{\frac{1}{m}} \mathrm{sgn} \left(\tau^{\alpha} \right)$$
(9)

where $\dot{\gamma}_0$ is the reference slip rate, m is the instantaneous strain rate sensitivity and τ_c^{α} is the history dependent critical resolved shear stress of slip system α. The initial value of the yield strength is equal to $\tau_c^{\alpha} = \tau_y$ for all slip systems.

We introduce work-hardening by connecting the critical resolved shear stress rate $\dot{\tau}_c^\alpha$ to the slip rates on the slip systems

$$\dot{\tau}_c^\alpha = \theta \sum_{\beta=1}^n q_{\alpha\beta} \left| \dot{\gamma}^\beta \right| \tag{10}$$

where $\theta \equiv d\tau_c / d\Gamma$ is the hardening modulus defined by a master curve, and $q_{\alpha\beta}$ is the matrix of self-hardening and latent-hardening coefficients. The accumulated slip Γ is defined by the evolution equation

$$\dot{\Gamma} = \sum_{\alpha=1}^n \left| \dot{\gamma}^\alpha \right| \tag{11}$$

The master hardening curve is given by an equation proposed in [8]

$$\tau_c = \tau_y + \alpha \mu b \sqrt{\rho_s + \rho_{g1} + \rho_{g2}} \tag{12}$$

where ρ_s is the statistically stored dislocation (SSD) density, responsible for the forest hardening, and ρ_{g1} and ρ_{g2} are the geometrically necessary dislocation (GND) densities associated with different physical mechanisms. One must distinguish between the "real" GNDs and the parameters of the present model. The "real" GNDs are generated by the plastic strain gradient, while here everything is controlled by the plastic strain. The reason why this designation is used is that the zones where ρ_{g1} and ρ_{g2} are increasing are chosen in such a way that some plastic strain heterogeneity will always be present in them under plastic deformation. This approach originates from [32] and is continued in [69].

The dislocation density evolutions are connected to the accumulated slip by

$$d\rho_s = \left(k_1 \sqrt{\rho_s} - k_2 \rho_s \right) d\Gamma \tag{13}$$

$$d\rho_{g1} = \frac{1}{bL_1} \left(1 - \left(\frac{\rho_{g1}}{\rho_{g1}^{sat}} \right)^a \right) d\Gamma \tag{14}$$

$$d\rho_{g2} = \frac{1}{bL_2} d\Gamma \tag{15}$$

where k_1 and k_2 are in turn the accumulation and annihilation coefficients for statistically stored dislocations [10], L_1 is the characteristic length proportional to the average distance between the non-shearable precipitate particles [32] and L_2 is the characteristic length associated with the dislocation accumulation in the pile-ups near the PFZs. As described above, the dislocation accumulation around the non-shearable precipitate particles is limited by some mechanisms and saturates at some value. ρ_{g1}^{sat} is the density of geometrically necessary dislocations at saturation. The parameter a allows for a smooth saturation of the density and its value is here chosen to be equal to 10. The work-hardening modulus θ is the derivative of the master curve τ_c with respect to the accumulated slip Γ, viz.

$$\theta \equiv \frac{d\tau_c}{d\Gamma} = \frac{\partial \tau_c}{\partial \rho_s} \frac{d\rho_s}{d\Gamma} + \frac{\partial \tau_c}{\partial \rho_{g1}} \frac{d\rho_{g1}}{d\Gamma} + \frac{\partial \tau_c}{\partial \rho_{g2}} \frac{d\rho_{g2}}{d\Gamma} \tag{16}$$

which by use of Equations (12)-(15) may be rewritten as

$$\theta = \frac{\alpha \mu b}{2\sqrt{\rho_s + \rho_{g1} + \rho_{g2}}} \left(k_1 \sqrt{\rho_s} - k_2 \rho_s + \frac{1}{bL_1} \left(1 - \left(\frac{\rho_{g1}}{\rho_{g1}^{sat}} \right)^a \right) + \frac{1}{bL_2} \right) \tag{17}$$

The initial dislocation density in the undeformed material is very low compared to the deformed material as may be seen in the TEM photographs in Section 2, though not zero. In the numerical model all the dislocation density variables were initiated at a value of 10 mm^{-2}. At the end of the simulations the densities reached values of the order of 10^7 mm^{-2}. The exact value used for the initialization was of no consequence for the results of the simulations.

5. Parameters of the constitutive model

The material properties of the AA6000 series Al alloys were used as a reference when selecting the values of the model parameters. The parameters describing the elastic properties of the material, the reference slip rate, the rate sensitivity, and the latent hardening coefficients are common for all Al alloys and may be found in the literature. These values are given in Table 2. The values of the hardening parameters were calculated using the method described in [34] and [65] for the AA6060 alloy in T6 temper. The resulting stress-strain curve does not necessarily fit the experimental one exactly, but for the purpose of this work it was more important to obtain hardening parameters typical for a peak-aged alloy with PFZs

than to accurately fit a specific curve. The aforementioned method allowed estimating the microstructure-related parameters, such as dislocation accumulation and annihilation coefficients and the non-shearable precipitate spacing in a convenient manner without complex experimental procedures. The obtained values of the hardening parameters are presented in Table 3.

As may be seen from Table 3, the bulk of the grain and the pile-up zone have common hardening mechanisms, namely accumulation and recovery of statistically stored dislocations and accumulation of geometrically necessary dislocations around non-shearable precipitate particles, and consequently share the values of the corresponding parameters. The additional characteristic length for the pile-up zone is difficult to estimate. One way is to calculate the average dislocation production rate in the PFZ and assume that around half of these dislocations will be stored in the pile-up. This neglects the annihilation process, but at least provides an estimate. The value in the table is chosen after some preliminary simulations, based on this assumption. According to [34] the dislocation production coefficient k_1 is a constant for a given family of alloys, so it is chosen to be constant for all three zones. For the PFZ, the parameter k_2 is chosen to be higher than for the other two zones, which here does not mean a high rate of annihilation, but rather implies that the dislocations leave the zone and do not accumulate in it, leading effectively to almost perfect plastic behaviour. Figure 13 presents the slip resistance τ_c plotted against the accumulated slip Γ for the three zones.

6. Numerical study

The FEM was used to study the behaviour of the described crystalline composite material system. The model in Figure 10 was represented by a 2D finite element mesh, see Figure 14. The nonlinear FEM code LS-DYNA [70] was used in the calculations. The crystal plasticity material model was implemented as a user-material subroutine, using the explicit integration scheme by Grujicic and Batchu [71]. Four-node plane-strain quadrilateral elements with reduced integration and Flanagan-Belytschko stiffness-based hourglass control were used. The explicit solver of LS-DYNA was adopted and correspondingly explicit integration of the momentum equations was used. Mass-scaling was applied to reduce the computation time and the kinetic energy was controlled at every step to ensure that it was very small compared to the total energy and that the simulation remained quasi-static. The grain structure of the FEM model is periodic and periodic boundary conditions were applied on the edges of the mesh. In

the simulations, the model was subjected to plane-strain tension in the *x*-direction by applying a velocity smoothly ramping up to a constant value to the corner node.

The recrystallized microstructure was stretched to approximately 10% engineering strain and the fibrous microstructure to 15%. The limiting factor in the simulations was the extreme deformations in the PFZ leading to quick decrease of the time step. The deformed meshes of the composite and homogeneous models of the two microstructures are shown in Figure 15. The deformation patterns presented in these two figures are noticeably different. The composite model demonstrates large shear deformation in a number of PFZs, leading to grains sliding relative to each other. The sliding causes distortion of the grain boundary near the grain boundary triple points. The grain boundaries mainly distort as a result of a passing shear band in the homogeneous model. The overall shape of the deformed microstructure is not exactly the same between the composite and homogeneous models, but it is still somewhat similar, due to the same crystallographic orientations of the constituent grains.

Contour plots of the von Mises plastic strain are shown in Figure 16. The plastic strain distribution is highly inhomogeneous in both the composite and homogeneous models. The highest plastic strain in the composite model is reached within the PFZs. Its maximum value reaches around 8.0. Therefore to improve the readability of the contour plot and for comparison with the homogeneous model, the maximum strain of the colour bar is chosen to be smaller. For the homogeneous model, the highest value of approximately 0.7 is reached within the shear band. The shear bands are the most prominent feature in the contour plots of the equivalent plastic strain. In the homogeneous model of both the recrystallized and fibrous structures, several larger shear bands cross multiple grains. For the composite model, the shear bands are always nucleated by the shearing of a favourably oriented PFZ, i.e., a PFZ that makes about a 45° angle with the tensile axis. The bands propagate through the grains, they are sometimes stopped at the pile-up layer of the grain or they connect to another shearing PFZ or another band. If only the grain interior is considered in the composite model, then the equivalent plastic strain levels are similar to the ones observed in the homogeneous model.

The large plastic strains in the crystalline PFZ lead to large rotations of the lattice in the PFZ. Figure 17 shows the contour plot of the first Euler angle φ_1 in one of the highly deformed PFZs in the recrystallized model. The angle is high enough for the PFZ to become a

subgrain-like band structure, which may be compared to a similar structure from the TEM study in Figure 8.

The mesh influence on the mechanical fields inside the grains was studied by testing a model, similar to the composite model in Figure 10, but with refined mesh inside one of the grains. Refining the mesh for the whole model would lead to a prohibitively long FEM simulation. The von Mises plastic strain contours inside this grain for the coarse mesh and the refined mesh are shown in Figure 18. The refined mesh did not predict any new or different features neither in the grain nor in its neighbours. The plastic strain levels in the coarse and refined meshes are also similar.

Figure 19 presents contour plots of the von Mises stress. The homogeneous model presents a typical distribution, where the grains with harder and softer orientations reach correspondingly higher and lower levels of stress. The composite model again demonstrates a very different distribution. The stress within the grains is varying, again at the levels comparable to the homogeneous model, but the variations are overshadowed by the stress concentrations that arise in the pile-up zones. The highest stress concentrations are associated predictably with the distorted grain boundaries, where the stress reaches up to 400-500 MPa. Figure 20 shows the details of the distribution in a part of the composite model around a triple point. Once again the maximum value of the colour bar is the same for the homogeneous and the composite model for comparison and to improve the readability. Where the grain boundaries remained undistorted, the stress level is similar to the one in the grain interior. The PFZs have no means to work-harden and increase their stress, so the stress level in these zones is consistently low.

Figure 21 shows contour plots of the hydrostatic pressure. The distribution of the pressure in the homogeneous model is defined by the constraint that the grains with harder orientations impose on the grains with softer orientations. In the composite model, the distribution is again more heterogeneous. The PFZs oriented normally to the tensile axis are subjected to the same load as the rest of the grain but cannot slide. The hydrostatic pressure is the only way for these PFZs to carry the load and therefore they exhibit the highest negative pressure. The zones of highest positive hydrostatic pressure are positioned near the triple junctions of the grain boundaries, where the pile-up zones are subjected to strong distortion and generate strong stress fields. In some cases the high pressure fields propagate inside the grain interior. The PFZs that are oriented obliquely to the tensile axis are all shearing to some

degree, which allows them to relax the constraint imposed by the grains and reduce the hydrostatic stress component. The contour plots of the stress triaxiality in Figure 22 reveal yet another trend. The low deviatoric and high hydrostatic stresses in the PFZs normal to the tensile axis lead to excessively high triaxiality values in these regions. The zones of high negative triaxiality are again associated with the grain boundary distortion at the triple junction points. The range of the contour plot is again the same for the homogeneous and the composite model, with maximum/minimum values taken from the homogeneous model.

The distribution of the geometrically necessary dislocation densities ρ_{g1} and ρ_{g2} in the model of the recrystallized microstructure is shown in Figure 23. The GNDs in the homogeneous model follow the distribution of the plastic strain, which is reasonable both numerically and physically, as it corresponds to the dislocation accumulation around the non-shearable precipitates with increasing plastic deformation. For the composite model the GNDs accumulate in large numbers in the pile-up zones. The levels of GND densities inside the grain interior are once again similar for the two models, although the distribution of the densities is different.

Figure 24 shows the engineering stress-strain curves for the composite and homogeneous models. While the yield stress is reduced by the presence of PFZs, the work-hardening rate before and after maximum force is reached is very similar for these two models. Large local deformations in the shear bands and in the PFZs are limited in extent and do not lead to a global loss of load-carrying capacity. One must remember that the periodic patches of material, like the ones used in this work, are not necessarily most suited for the study of localisation bands and the global load-carrying capacity, and may prevent the natural propagation of the shear bands, see [72] for a detailed discussion. Nevertheless in the present work only the numerical models with similar periodic constraints are used, which should make at least a qualitative comparison meaningful.

7. Discussion

One of the most noticeable details in the performed simulations is the extremely large plastic strains reached by some finite elements in the PFZs. On one hand, it may seem like a cause of concern, but on the other hand, there are no indications that any sort of numerical problem is associated with the large strains except the decreasing time step. The deformation mode of the corresponding elements is a basic combination of shear and stretch. The slip activity, stress

calculations and energy balance in the model are ordinary and predictable despite the large strains. The exact distribution of the plastic strains in the real PFZ under deformation is not clear. Experiments presented in [56] show that the neighbouring grains divided by a GB with a PFZ may shift significantly relative to each other, which corresponds to very high average strain in the PFZ. Still, the exact local distribution of this strain inside the PFZ is not known. In the FEM model the same trend of grains shifting relative to each other is observed. The maximum local plastic strain inside the PFZ in turn depends on the width of the PFZ relative to the grain and the mesh resolution inside it, as some additional simulations have shown. Thus one should be careful interpreting the local results of the simulations inside the PFZs. On the other hand the global behaviour of the PFZ part of the model is a reasonable approximation to the existing experimental observations.

The contour plots of the hydrostatic pressure demonstrated a checkerboard pattern locally in both the recrystallized and fibrous composite model, see Figure 25. The pattern is localized around the highly deformed zones and has very limited extent. The checkerboard patterns are a sign of volumetric locking, which is quite common in the FE analysis of the plastic incompressible materials [73-75], especially in case of simple linear elements, such as tetrahedral or triangular. These studies also show that a more advanced element formulation could alleviate this problem, at an increased computational cost. It is unlikely that these patterns had a strong effect on the solution, since the plasticity is driven by deviatoric stresses. But this may become a more serious problem if ductile damage is included into the crystal plasticity formulation, because the damage evolution is known to depend strongly on the stress triaxiality.

The shear bands in the homogeneous models arise naturally as a material instability. While the understanding of their physical nature is still improved, e.g. by [76], they have been observed in the crystal plasticity FEM simulations since the first works on this topic, like [77]. The shear bands in the composite model were produced by the constraint caused by the sliding of the neighbouring grains, usually near the triple junction points. Whether a shear band would be produced or not depended also on the crystallographic orientation of the deformed grain. Some orientations were more favourable to the shear-band formation and propagation than others. Figure 26 shows the contour plot of the von Mises plastic strain of the composite model of the recrystallized microstructure, which is equivalent to the model in Figure 16 in every aspect except for the crystallographic orientations of the grains. The new orientations are a different randomly generated set. The shear bands formed in these two cases

are very different despite a similarity in the constraint that leads to their formation. The formation of the shear bands at a triple junction in Al polycrystals, similar to what the composite model produced, was observed in [49].

The PFZs in the composite model were assigned almost perfect plastic behaviour, as discussed in Section 5. If some work-hardening mechanism was assigned to the PFZs instead, the results would depend on how close and how fast this work-hardening may strengthen the PFZ to the level of the grain interior. The simulation of the composite model of the recrystallized microstructure was run with a value of parameter $k_2 = 4.6$ (corresponding to a solution heat-treated alloy in T4 temper), which allowed it to harden almost to the level of the grain interior, see Figure 13. The contour plot of the von Mises plastic strain for this simulation is shown in Figure 27. The maximum plastic strain in the PFZs is still very high, reaching a value of 1.3, but much lower than in the non-hardening case. The plastic strain distribution is very similar to the homogeneous model. The shear bands only form in the same location as in the homogeneous model, because the triple point initiation mechanism is not functioning. From this simulation it may be seen that due to the very small width of the PFZ and the high plastic strains that arise very quickly in them during the deformation, the lower yield stress is not as important for the later stages of deformation as some work-hardening mechanism can sufficiently strengthen them.

The representation of the pile-up zone in the composite model is a rather crude approximation. Its main problem is that it hardens depending on its own deformation, instead of hardening because of the deformation of the PFZ and the dislocations exiting from the PFZ. In most cases this approach still worked, because the grain boundaries in such a model tend to distort. This distortion lead to dislocation accumulation and still made the pile-up zone the strongest part of the grain. A better result could possibly have been obtained with a strain gradient plasticity model, but it would likely lead to a prohibitively high computation time for a FEM model with the required level of detail.

8. Conclusions

The finite element method was employed to study a model of a polycrystal with heterogeneous yield and work-hardening properties. The structure of the model and the material properties were chosen based on the pre-existing literature and new experimental study results. The experimental study was performed on the AA6060 alloy in T6 temper.

TEM samples were produced from a deformed tensile specimen at different locations, corresponding to different levels of plastic strain. PFZs were identified in these samples and their structure at different levels of global plastic straining was studied. The observations of the dislocation behaviour in and around the PFZs were used as a basis for the composition of the polycrystal model. Each grain of the polycrystals included three zones: one narrow soft zone with low yield stress and nearly vanishing work-hardening rate, one narrow stronger zone with high yield stress and high work-hardening rate, and the broadest zone with high yield stress and low work-hardening rate. A single crystal plasticity model was used to describe the material behaviour. The dislocation density was the parameter that controlled the work-hardening of the single crystal plasticity model, and its evolution reflected the experimental observations. The model mimicked an Al alloy with either recrystallization or fibrous microstructure. The 2D FEM models of the composite polycrystals were subjected to plane-strain tension loading.

The displacement and strain fields obtained from the simulations showed some distinct features of this kind of a crystalline composite, including sliding of the grains along the soft zones favourably oriented relative to the tensile axis, grain boundary distortion, especially in the triple junction points, shear band initiation and propagation, due to the grain sliding in some grains with favourable crystallographic orientations. The stress calculations in the simulations produced distributions of plastic strain and deviatoric and hydrostatic stresses in the composite polycrystals which are very different from the more traditional polycrystal model with homogeneous grains.

The finite element models of the crystalline composite presented in this work are based on several crude approximations, and also making some assumptions about the properties and behaviour of the crystals in and around precipitate-free zones that may be unconventional. The results show that these approximations and assumptions are at least partly reasonable. If one aims to describe the local mechanical fields in the artificially aged Al polycrystals, e.g. to predict the initiation and evolution of the ductile damage, one can ignore neither the presence of precipitate-free zones nor their crystalline nature.

Acknowledgment

References

[1]   A. Saai, S. Dumoulin, and O. Hopperstad, "Influence of texture and grain shape on the yield surface in aluminium sheet material subjected to large deformations," in *AIP Conference Proceedings*, 2011, p. 85.

[2]   S. Dumoulin, O. Engler, O. Hopperstad, and O. Lademo, "Description of plastic anisotropy in AA6063-T6 using the crystal plasticity finite element method," *Modelling and Simulation in Materials Science and Engineering,* vol. 20, p. 055008, 2012.

[3]   M. Khadyko, S. Dumoulin, G. Cailletaud, and O. Hopperstad, "Latent hardening and plastic anisotropy evolution in AA6060 aluminium alloy," *International Journal of Plasticity,* vol. 76, pp. 51-74, 2016.

[4]   M. Khadyko, S. Dumoulin, T. Børvik, and O. Hopperstad, "An experimental-numerical method to determine the work-hardening of anisotropic ductile materials at large strains," *International Journal of Mechanical Sciences,* vol. 88, pp. 25-36, 2014.

[5]   K. Zhang, B. Holmedal, O. Hopperstad, and S. Dumoulin, "Modelling the plastic anisotropy of aluminum alloy 3103 sheets by polycrystal plasticity," *Modelling and Simulation in Materials Science and Engineering,* vol. 22, p. 075015, 2014.

[6]   K. Zhang, B. Holmedal, O. S. Hopperstad, S. Dumoulin, J. Gawad, A. Van Bael, and P. Van Houtte, "Multi-level modelling of mechanical anisotropy of commercial pure aluminium plate: crystal plasticity models, advanced yield functions and parameter identification," *International Journal of Plasticity,* vol. 66, pp. 3-30, 2015.

[7]   H. Zhang, M. Diehl, F. Roters, and D. Raabe, "A virtual laboratory using high resolution crystal plasticity simulations to determine the initial yield surface for sheet metal forming operations," *International Journal of Plasticity,* vol. 80, pp. 111-138, 2016.

[8]   G. I. Taylor, "The Mechanism of Plastic Deformation of Crystals. Part I. Theoretical," *Proceedings of the Royal Society of London. Series A,* vol. 145, pp. 362-387, July 2, 1934 1934.

[9]   U. Kocks, "Laws for work-hardening and low-temperature creep," *Journal of Engineering Materials and Technology,* vol. 98, p. 76, 1976.

[10]   H. Mecking and U. Kocks, "Kinetics of flow and strain-hardening," *Acta Metallurgica,* vol. 29, pp. 1865-1875, 1981.

[11]   D. Kuhlmann-Wilsdorf, "Theory of workhardening 1934-1984," *Metallurgical Transactions A,* vol. 16, pp. 2091-2108, 1985.

[12]   S. C. Baik, Y. Estrin, H. S. Kim, and R. J. Hellmig, "Dislocation density-based modeling of deformation behavior of aluminium under equal channel angular pressing," *Materials Science and Engineering: A,* vol. 351, pp. 86-97, 2003.

[13]   C. Hamelin, B. Diak, and A. Pilkey, "Multiscale modelling of the induced plastic anisotropy in bcc metals," *International Journal of Plasticity,* vol. 27, pp. 1185-1202, 2011.

[14]   X. Fan, H. Yang, and P. Gao, "Prediction of constitutive behavior and microstructure evolution in hot deformation of TA15 titanium alloy," *Materials & Design,* vol. 51, pp. 34-42, 2013.

[15]   N. Bertin, L. Capolungo, and I. Beyerlein, "Hybrid dislocation dynamics based strain hardening constitutive model," *International Journal of Plasticity,* vol. 49, pp. 119-144, 2013.

[16]   M. Knezevic, R. J. McCabe, R. A. Lebensohn, C. N. Tomé, C. Liu, M. L. Lovato, and B. Mihaila, "Integration of self-consistent polycrystal plasticity with dislocation density based hardening laws within an implicit finite element framework: application to low-symmetry metals," *Journal of the Mechanics and Physics of Solids,* vol. 61, pp. 2034-2046, 2013.

[17]   D. Li, H. Zbib, X. Sun, and M. Khaleel, "Predicting plastic flow and irradiation hardening of iron single crystal with mechanism-based continuum dislocation dynamics," *International Journal of Plasticity,* vol. 52, pp. 3-17, 2014.

[18]   P. Engels, A. Ma, and A. Hartmaier, "Continuum simulation of the evolution of dislocation densities during nanoindentation," *International Journal of Plasticity,* vol. 38, pp. 159-169, 2012.

[19]   P. Shanthraj and M. A. Zikry, "Dislocation density evolution and interactions in crystalline materials," *Acta materialia,* vol. 59, pp. 7695-7702, 2011.

[20]   M. Lee, H. Lim, B. Adams, J. Hirth, and R. Wagoner, "A dislocation density-based single crystal constitutive equation," *International Journal of Plasticity,* vol. 26, pp. 925-938, 2010.

[21] J. Li and A. Soh, "Modeling of the plastic deformation of nanostructured materials with grain size gradient," *International Journal of Plasticity,* 2012.

[22] H. Lim, M. Lee, J. Kim, B. Adams, and R. Wagoner, "Simulation of polycrystal deformation with grain and grain boundary effects," *International Journal of Plasticity,* vol. 27, pp. 1328-1354, 2011.

[23] T. C. Resende, S. Bouvier, F. Abed-Meraim, T. Balan, and S.-S. Sablin, "Dislocation-based model for the prediction of the behavior of bcc materials– grain size and strain path effects," *International Journal of Plasticity,* vol. 47, pp. 29-48, 2013.

[24] N. Bertin, C. Tomé, I. Beyerlein, M. Barnett, and L. Capolungo, "On the strength of dislocation interactions and their effect on latent hardening in pure Magnesium," *International Journal of Plasticity,* vol. 62, pp. 72-92, 2014.

[25] F. Barlat, J. Ha, J. J. Grácio, M.-G. Lee, E. F. Rauch, and G. Vincze, "Extension of homogeneous anisotropic hardening model to cross-loading with latent effects," *International Journal of Plasticity,* vol. 46, pp. 130-142, 2013.

[26] M. Knezevic, I. J. Beyerlein, D. W. Brown, T. A. Sisneros, and C. N. Tomé, "A polycrystal plasticity model for predicting mechanical response and texture evolution during strain-path changes: application to beryllium," *International Journal of Plasticity,* vol. 49, pp. 185-198, 2013.

[27] G. Lemoine, L. Delannay, H. Idrissi, M.-S. Colla, and T. Pardoen, "Dislocation and back stress dominated viscoplasticity in freestanding sub-micron Pd films," *Acta materialia,* vol. 111, pp. 10-21, 2016.

[28] Z. Liu, Z. Zhuang, X. Liu, X. Zhao, and Z. Zhang, "A dislocation dynamics based higher-order crystal plasticity model and applications on confined thin-film plasticity," *International Journal of Plasticity,* vol. 27, pp. 201-216, 2011.

[29] P. Shanthraj and M. A. Zikry, "Dislocation-density mechanisms for void interactions in crystalline materials," *International Journal of Plasticity,* vol. 34, pp. 154-163, 2012.

[30] L. Lecarme, C. Tekog, and T. Pardoen, "Void growth and coalescence in ductile solids with stage III and stage IV strain hardening," *International Journal of Plasticity,* vol. 27, pp. 1203-1223, 2011.

[31] M. Ardeljan, I. J. Beyerlein, and M. Knezevic, "A dislocation density based crystal plasticity finite element model: Application to a two-phase polycrystalline HCP/BCC composites," *Journal of the Mechanics and Physics of Solids,* vol. 66, pp. 16-31, 2014.

[32] M. Ashby, "The deformation of plastically non-homogeneous materials," *Philosophical Magazine,* vol. 21, pp. 399-424, 1970.

[33] K. G. Russell and M. Ashby, "Slip in aluminum crystals containing strong, plate-like particles," *Acta Metallurgica,* vol. 18, pp. 891-901, 1970.

[34] O. R. Myhr, Ø. Grong, and K. O. Pedersen, "A Combined Precipitation, Yield Strength, and Work Hardening Model for Al-Mg-Si Alloys," *Metallurgical and Materials Transactions A,* vol. 41, pp. 2276-2289, 2010.

[35] S. Forest and R. Sedláček, "Plastic slip distribution in two-phase laminate microstructures: dislocation-based versus generalized-continuum approaches," *Philosophical Magazine,* vol. 83, pp. 245-276, 2003.

[36] C. F. O. Dahlberg and P. Gudmundson, "Hardening and softening mechanisms at decreasing microstructural length scales," *Philosophical Magazine,* vol. 88, pp. 3513-3525, 2008.

[37] N. Cordero, A. Gaubert, S. Forest, E. P. Busso, F. Gallerneau, and S. Kruch, "Size effects in generalised continuum crystal plasticity for two-phase laminates," *Journal of the Mechanics and Physics of Solids,* vol. 58, pp. 1963-1994, 2010.

[38] H.-J. Chang, A. Gaubert, M. Fivel, S. Berbenni, O. Bouaziz, and S. Forest, "Analysis of particle induced dislocation structures using three-dimensional dislocation dynamics and strain gradient plasticity," *Computational Materials Science,* vol. 52, pp. 33-39, 2012.

[39] R. Sedláček and E. Werner, "Constrained shearing of a thin crystalline strip: Application of a continuum dislocation-based model," *Physical Review B,* vol. 69, p. 134114, 2004.

[40] V. Taupin, S. Berbenni, and C. Fressengeas, "Size effects on the hardening of channel-type microstructures: A field dislocation mechanics-based approach," *Acta Materialia,* vol. 60, pp. 664-673, 2012.

[41]   T. Ogura, S. Hirosawa, and T. Sato, "Quantitative characterization of precipitate free zones in Al–Zn–Mg (–Ag) alloys by microchemical analysis and nanoindentation measurement," *Science and Technology of Advanced Materials,* vol. 5, pp. 491-496, 2004.

[42]   M. Fourmeau, C. Marioara, T. Børvik, A. Benallal, and O. Hopperstad, "A study of the influence of precipitate-free zones on the strain localization and failure of the aluminium alloy AA7075-T651," *Philosophical Magazine,* pp. 1-27, 2015.

[43]   F. Scheyvaerts, P. Onck, Y. Bréchet, and T. Pardoen, "Multiscale simulation of the competition between intergranular and transgranular fracture in 7000 alloys," in *15th European Conference on Fracture: Advanced fracture Mechanics for Life and Safety Assessment*, 2004.

[44]   T. Pardoen and Y. Brechet, "Influence of microstructure-driven strain localization on the ductile fracture of metallic alloys," *Philosophical Magazine,* vol. 84, pp. 269-297, 2004.

[45]   T. Pardoen, F. Scheyvaerts, A. Simar, C. Tekoğlu, and P. R. Onck, "Multiscale modeling of ductile failure in metallic alloys," *Comptes Rendus Physique,* vol. 11, pp. 326-345, 2010.

[46]   T. Pardoen and T. J. Massart, "Interface controlled plastic flow modelled by strain gradient plasticity theory," *Comptes Rendus Mecanique,* vol. 340, pp. 247-260, 2012.

[47]   N. Ryum, "The influence of a precipitate-free zone on the mechanical properties of an Al-Mg-Zn alloy," *Acta Metallurgica,* vol. 16, pp. 327-332, 1968.

[48]   M. Abe, K. Asano, and A. Fujiwara, "Influence of the precipitate-free zone width on the tensile properties of an Al-6 Wt pct Zn-1.2 Wt pct Mg alloy," *Metallurgical Transactions,* vol. 4, pp. 1499-1505, 1973.

[49]   T. Kawabata and O. Izumi, "Ductile fracture in the interior of precipitate free zone in an Al-6.0% Zn-2.6% Mg alloy," *Acta Metallurgica,* vol. 24, pp. 817-825, 1976.

[50]   T. Kawabata and O. Izumi, "the relationship between fracture toughness and transgranular fracture in an Al-6.0% Zn-2.5% Mg alloy," *Acta Metallurgica,* vol. 25, pp. 505-512, 1977.

[51]   J. M. Dowling and J. Martin, "The influence of MN additions on the deformation behaviour of an Al Mg Si alloy," *Acta Metallurgica,* vol. 24, pp. 1147-1153, 1976.

[52] J.-W. Yeh and K.-S. Liu, "A study relating to the enhancement of transgranular fracture by iron in Al Zn Mg alloys," *Scripta Metallurgica,* vol. 20, pp. 329-334, 1986.

[53] P. Schwellinger, "On the fracture mechanisms in Al Mg Si-alloys," *Scripta Metallurgica,* vol. 14, pp. 769-772, 1980.

[54] D. Dumont, A. Deschamps, and Y. Brechet, "A model for predicting fracture mode and toughness in 7000 series aluminium alloys," *Acta Materialia,* vol. 52, pp. 2529-2540, 2004.

[55] T. Morgeneyer, M. Starink, S. Wang, and I. Sinclair, "Quench sensitivity of toughness in an Al alloy: Direct observation and analysis of failure initiation at the precipitate-free zone," *Acta Materialia,* vol. 56, pp. 2872-2884, 2008.

[56] O. Lohne and O. Naess, "The effect of dispersoids and grain size on mechanical properties of AlMgSi alloys," *Strength of Metals and Alloys.,* vol. 2, pp. 781-788, 1979.

[57] T. Krol, D. Baither, and E. Nembach, "The formation of precipitate free zones along grain boundaries in a superalloy and the ensuing effects on its plastic deformation," *Acta Materialia,* vol. 52, pp. 2095-2108, 2004.

[58] I. Groma, F. Csikor, and M. Zaiser, "Spatial correlations and higher-order gradient terms in a continuum description of dislocation dynamics," *Acta Materialia,* vol. 51, pp. 1271-1281, 2003.

[59] M. Zaiser and T. Hochrainer, "Some steps towards a continuum representation of 3d dislocation systems," *Scripta Materialia,* vol. 54, pp. 717-721, 2006.

[60] M. Zaiser, N. Nikitas, T. Hochrainer, and E. Aifantis, "Modelling size effects using 3D density-based dislocation dynamics," *Philosophical Magazine,* vol. 87, pp. 1283-1306, 2007.

[61] V. Tvergaard, A. Needleman, and K. K. Lo, "Flow localization in the plane strain tensile test," *Journal of the Mechanics and Physics of Solids,* vol. 29, pp. 115-142, 1981.

[62] N. Boudeau, J. Gelin, and S. Salhi, "Computational prediction of the localized necking in sheet forming based on microstructural material aspects," *Computational Materials Science,* vol. 11, pp. 45-64, 1998.

[63]   K. Inal, P. Wu, and K. Neale, "Instability and localized deformation in polycrystalline solids under plane-strain tension," *International Journal of Solids and Structures,* vol. 39, pp. 983-1002, 2002.

[64]   W. Zhuang, S. Wang, J. Lin, D. Balint, and C. Hartl, "Experimental and numerical investigation of localized thinning in hydroforming of micro-tubes," *European Journal of Mechanics-A/Solids,* vol. 31, pp. 67-76, 2012.

[65]   M. Khadyko, O. Myhr, S. Dumoulin, and O. Hopperstad, "A microstructure-based yield stress and work-hardening model for textured 6xxx aluminium alloys," *Philosophical Magazine,* pp. 1-26, 2016.

[66]   E. Lee and D. Liu, "Finite-Strain Elastic—Plastic Theory with Application to Plane-Wave Analysis," *Journal of Applied Physics,* vol. 38, pp. 19-27, 1967.

[67]   A. Needleman, R. Asaro, J. Lemonds, and D. Peirce, "Finite element analysis of crystalline solids," *Computer Methods in Applied Mechanics and Engineering,* vol. 52, pp. 689-708, 1985.

[68]   F. H. Norton, *The creep of steel at high temperatures*: McGraw-Hill Book Company, Incorporated, 1929.

[69]   I. Watanabe, D. Setoyama, N. Iwata, and K. Nakanishi, "Characterization of yielding behavior of polycrystalline metals with single crystal plasticity based on representative characteristic length," *International Journal of Plasticity,* vol. 26, pp. 570-585, 2010.

[70]   J. O. Hallquist, "LS-DYNA theory manual," *Livermore software technology corporation,* vol. 3, 2006.

[71]   M. Grujicic and S. Batchu, "Crystal plasticity analysis of earing in deep-drawn OFHC copper cups," *Journal of Materials Science,* vol. 37, pp. 753-764, 2002.

[72]   E. Coenen, V. Kouznetsova, and M. Geers, "Novel boundary conditions for strain localization analyses in microstructural volume elements," *International Journal for Numerical Methods in Engineering,* vol. 90, pp. 1-21, 2012.

[73]   E. Neto, F. Pires, and D. Owen, "F-bar-based linear triangles and tetrahedra for finite strain analysis of nearly incompressible solids. Part I: formulation and benchmarking," *International Journal for Numerical Methods in Engineering,* vol. 62, pp. 353-383, 2005.

[74] M. Gee, C. Dohrmann, S. Key, and W. Wall, "A uniform nodal strain tetrahedron with isochoric stabilization," *International Journal for Numerical Methods in Engineering,* vol. 78, pp. 429-443, 2009.

[75] J. Cheng, A. Shahba, and S. Ghosh, "Stabilized tetrahedral elements for crystal plasticity finite element analysis overcoming volumetric locking," *Computational Mechanics,* pp. 1-21, 2016.

[76] M. Kobayashi, "Analysis of deformation localization based on proposed theory of ultrasonic wave velocity propagating in plastically deformed solids," *International Journal of Plasticity,* vol. 26, pp. 107-125, 2010.

[77] D. Peirce, R. Asaro, and A. Needleman, "An analysis of nonuniform and localized deformation in ductile single crystals," *Acta Metallurgica,* vol. 30, pp. 1087-1119, 1982.

Figures
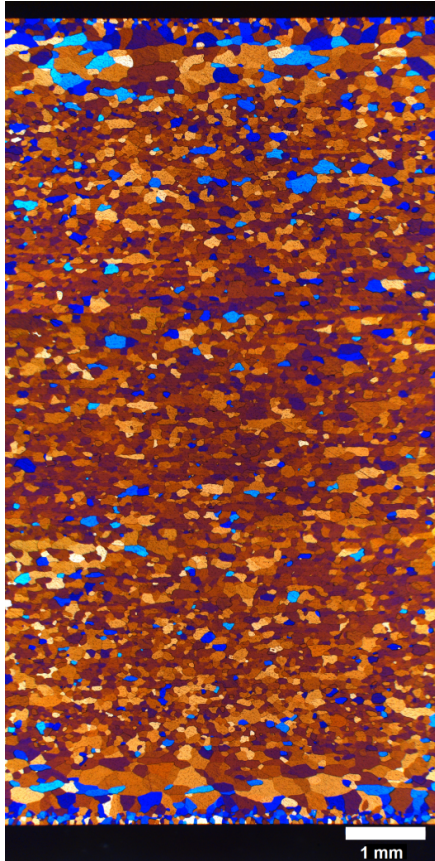
Figure 1: Grain structure of the AA6060 alloy, where the extrusion direction is horizontal and the normal (or thickness) direction is vertical [4].
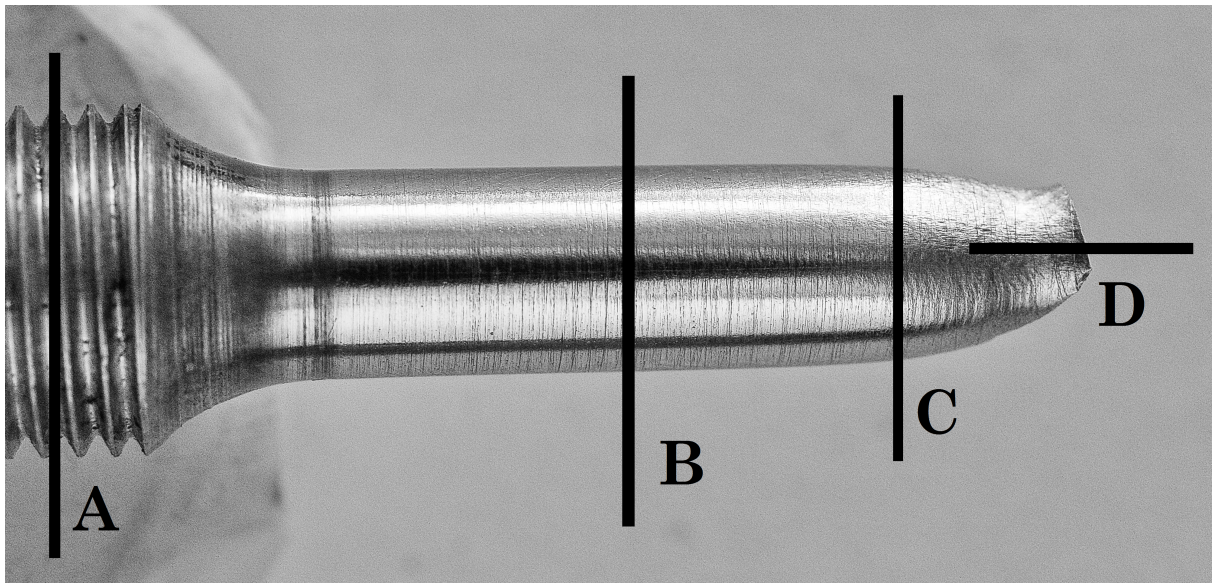
Figure 2: Locations on the tensile specimen, from which the TEM samples were produced.
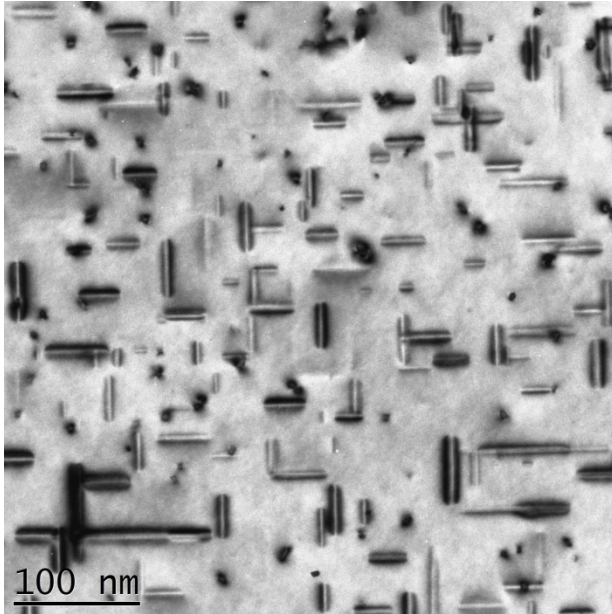
Figure 3: TEM bright field image of a typical bulk microstructure in the undeformed material (A section in Figure 2) characterised by a high number of homogeneously distributed needle-shaped precipitates oriented along <100>Al directions.
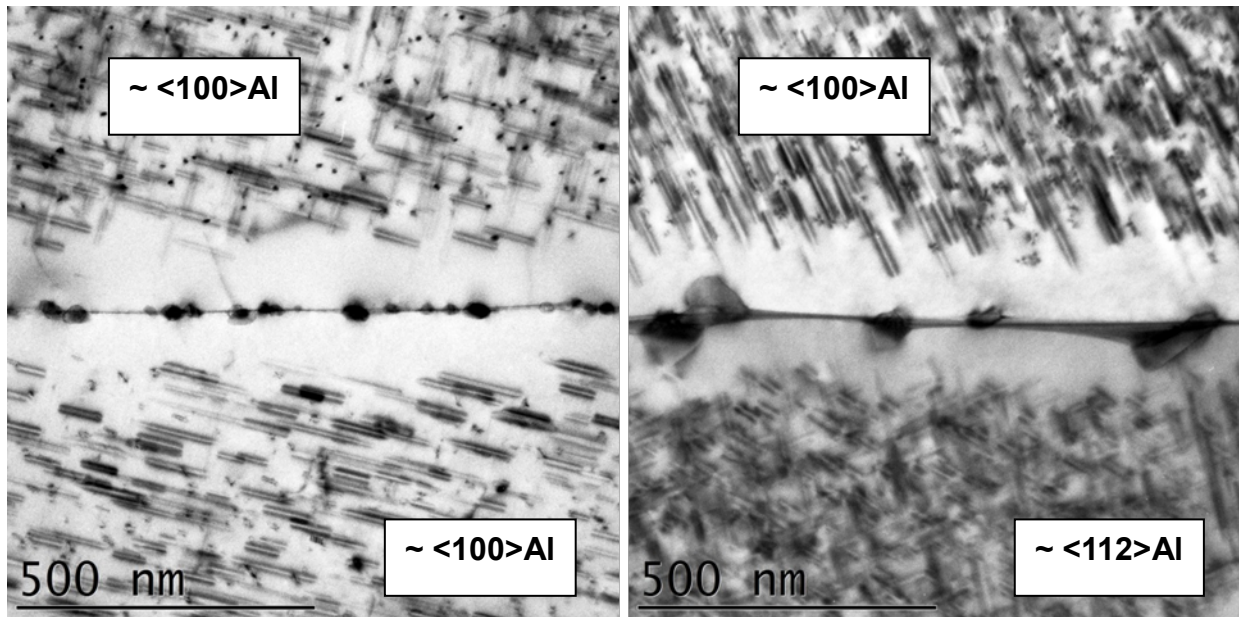
Figure 4: TEM bright field images of a) a low-angle GB and b) a high-angle GB in the undeformed material (A section in Figure 2). The approximate orientations of the grains along the viewing direction are indicated.
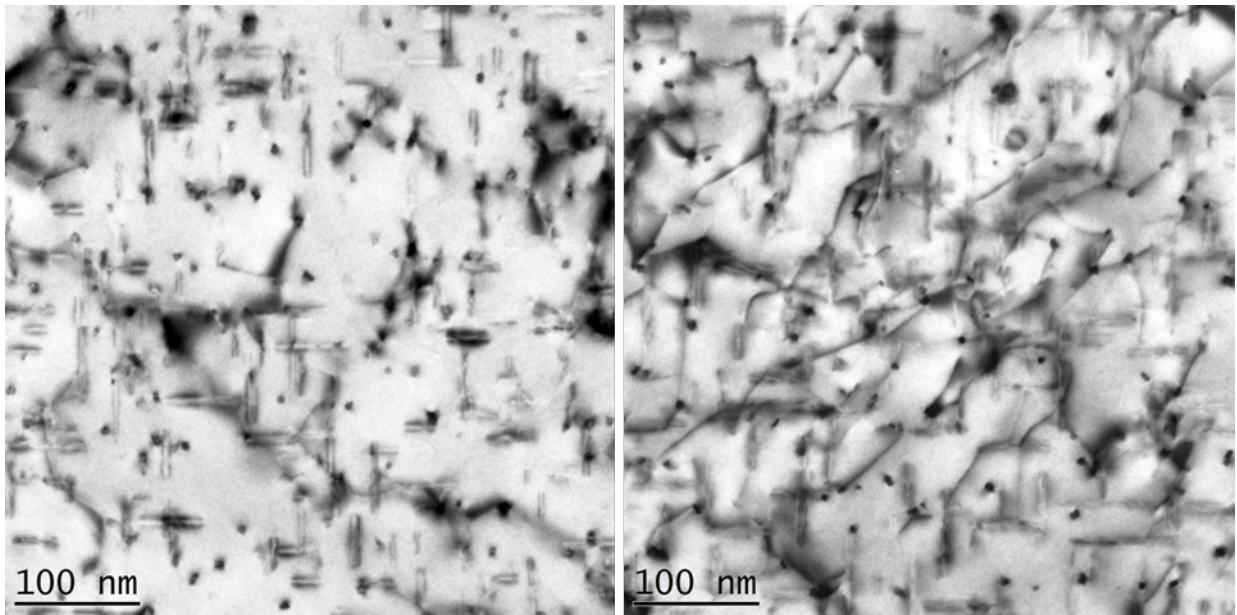
Figure 5: TEM bright field images of the deformed material outside the diffuse neck in the gauge area of the tensile sample (B section in Figure 2). Dislocations are observed interacting with needle precipitates in the bulk.
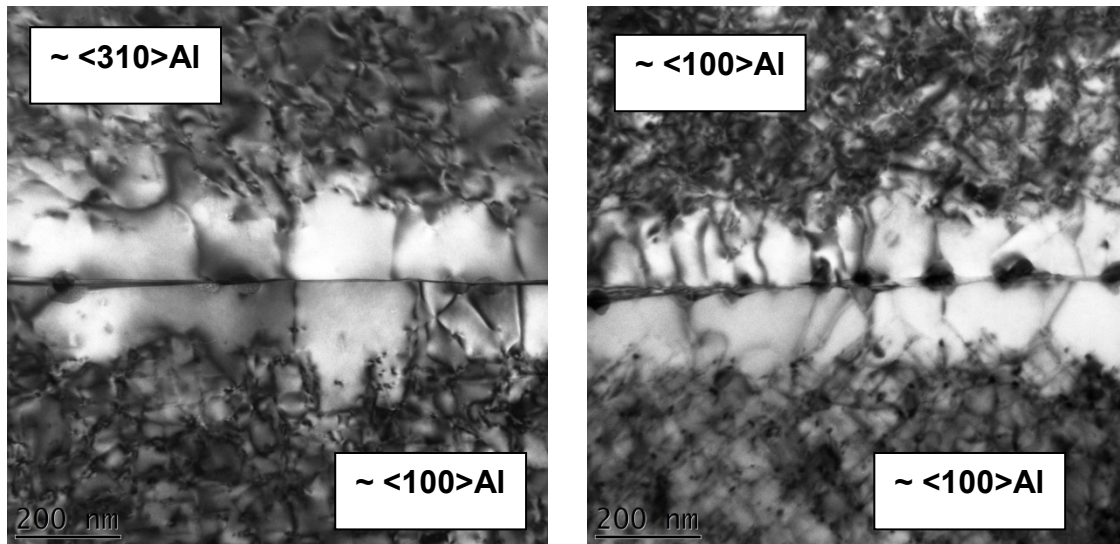
Figure 6: Bright field TEM images of GBs and PFZs in the deformed material outside the diffuse neck in the gauge area of the tensile sample (B section in Figure 2). The dislocation density is higher in the bulk than in the PFZs. In projection, the dislocations in the PFZs are oriented perpendicular to the GBs.
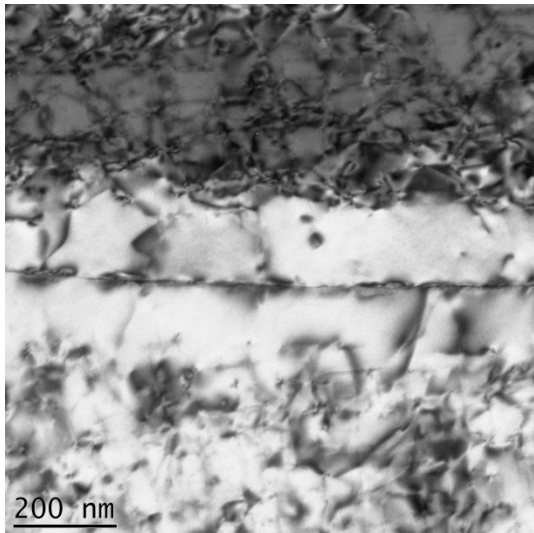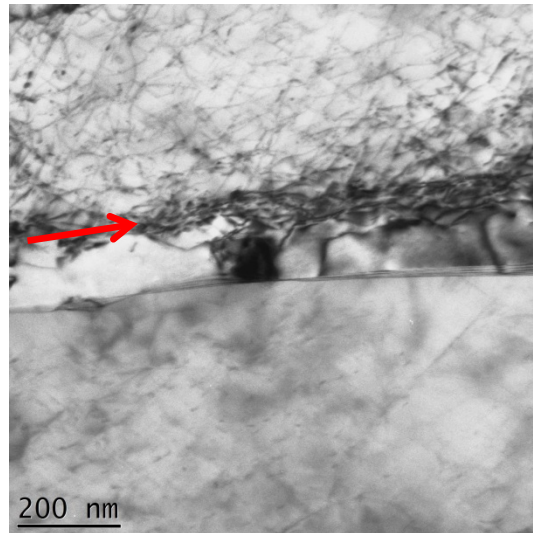
a)   b)

Figure 7: Bright field TEM images of GBs and PFZs in the deformed material inside the diffuse neck and close to the fracture surface (C section in Figure 2). In most cases these look similar to those outside the diffuse neck (a)), but sometimes dislocations pile-up along the transition zone between the grain interior and the PFZ. One such example is seen in b), where the pile-up is indicated by the red arrow.

a)   b)
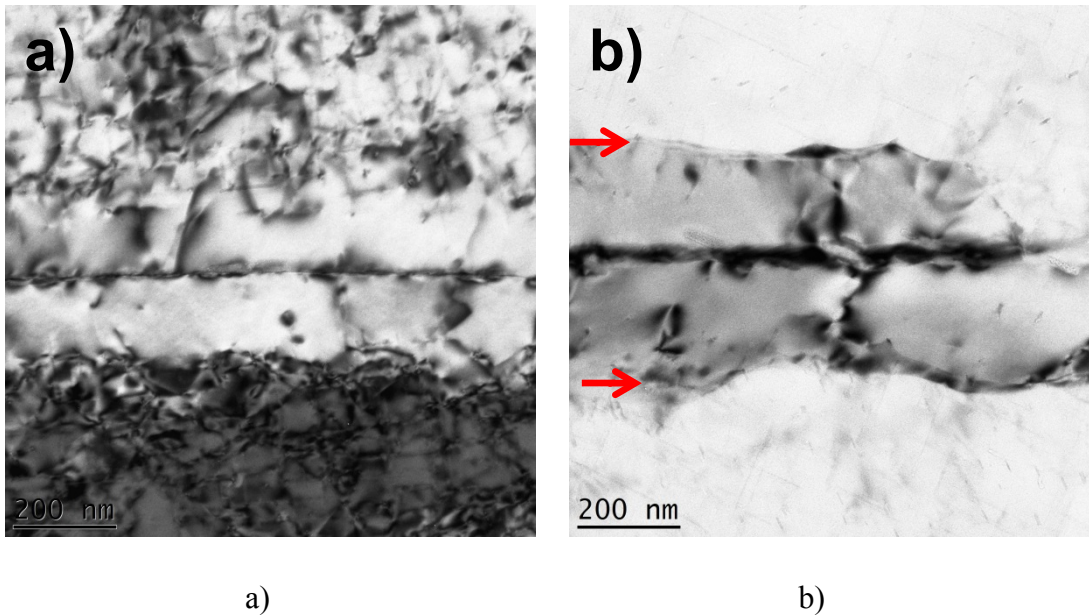
Figure 8: Bright field TEM images of GBs and PFZs in the deformed material inside the diffuse neck and close to the fracture surface (C section in Figure 2). Images a) and b) are from two different locations of the same GB, where a) shows a microstructure similar to Figure 6 and Figure 7 while in b) dislocation pile-ups form a wall close to and along the boundary between the grain interior and the PFZ. The pile-ups are indicated by red arrows.
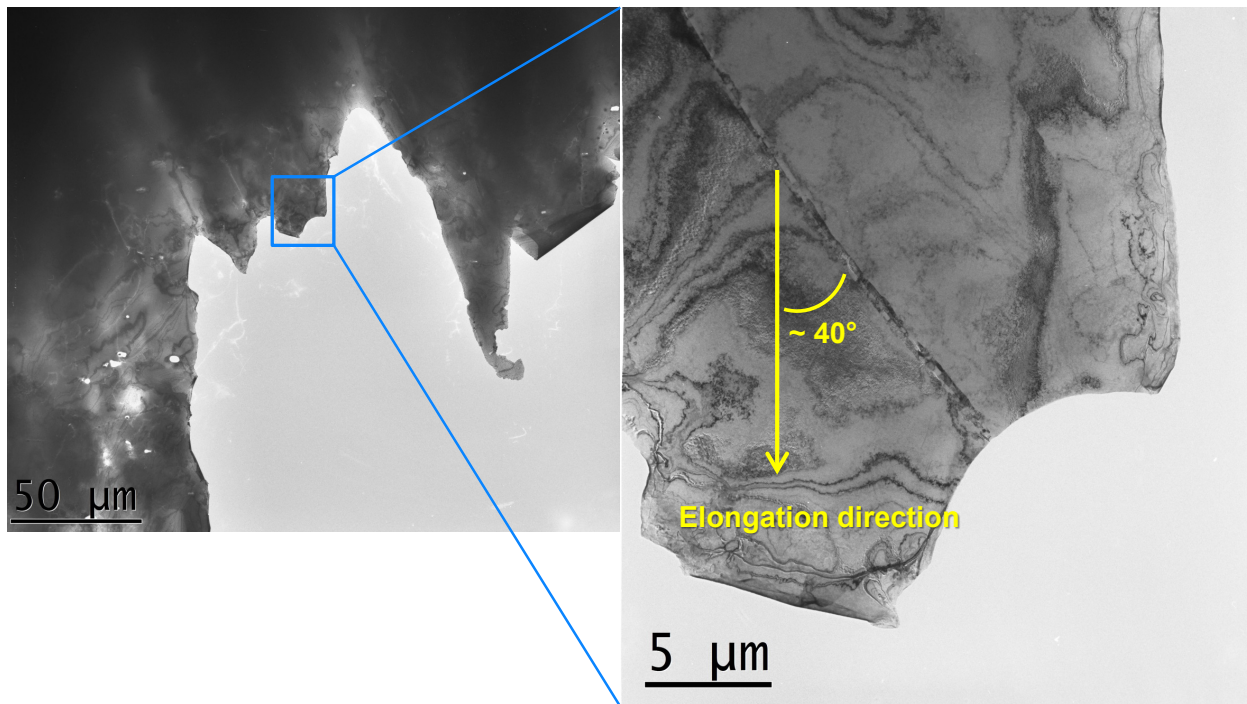
Figure 9: GB with band-like structure in the deformed material inside the neck and close to the fracture surface (D section in Figure 2) which makes an angle of approximately 40° with the elongation direction.
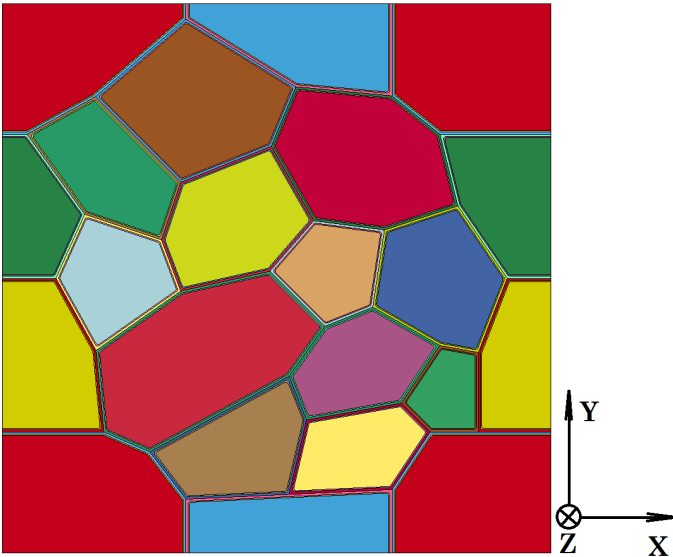
a)
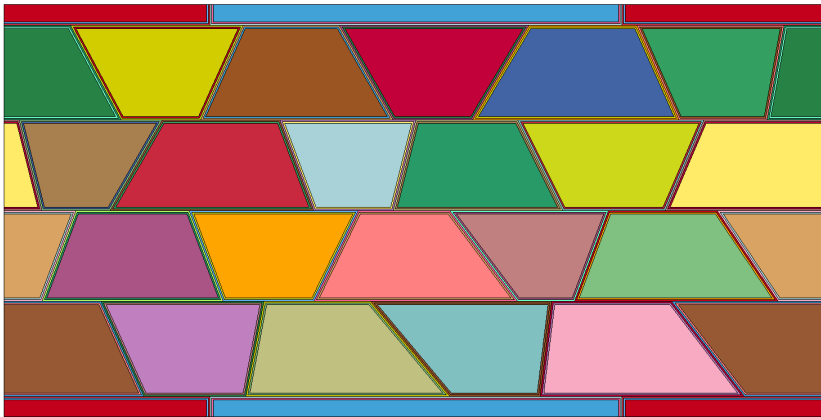
b)

Figure 10: Models of a) the recrystallized type and b) the fibrous type of polycrystals with a layered microstructure at the grain boundaries.
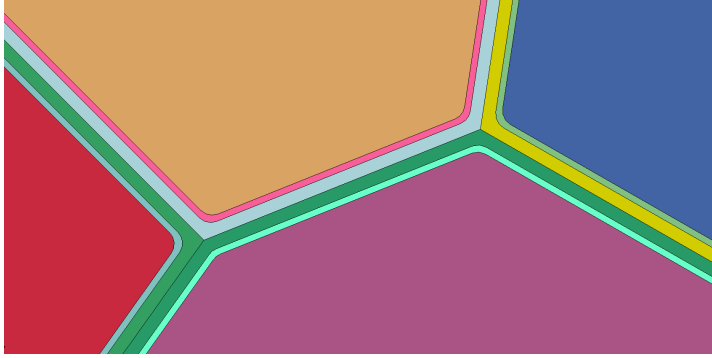
Figure 11: The layered structure between the grains of the polycrystal model.

a)   b)
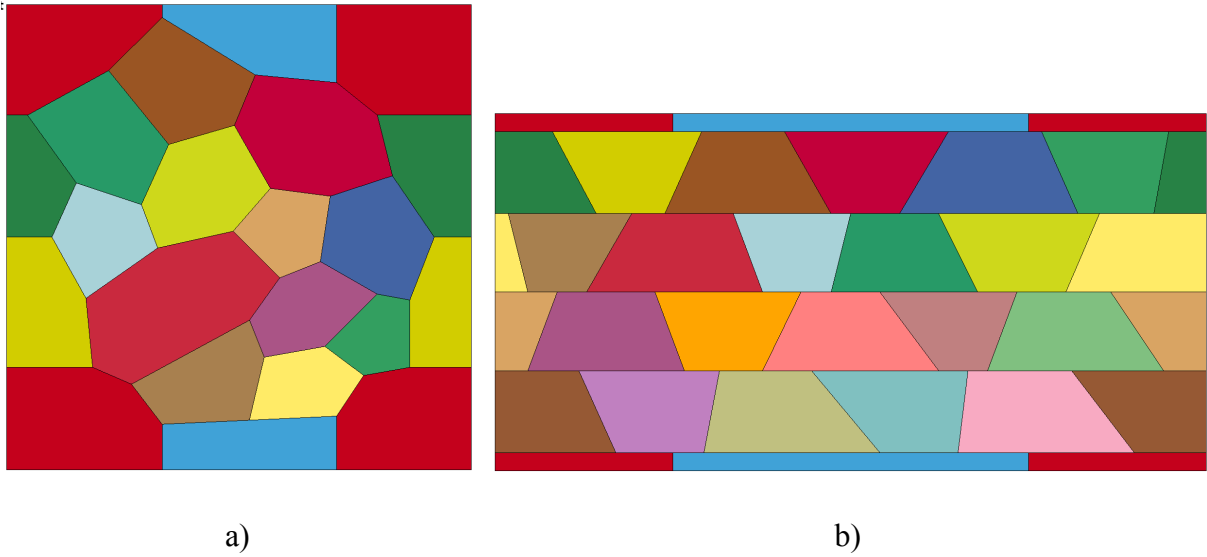
Figure 12: Model of the polycrystals without the layered microstructure on the grain boundaries: a) recrystallized type and b) fibrous type of polycrystals.
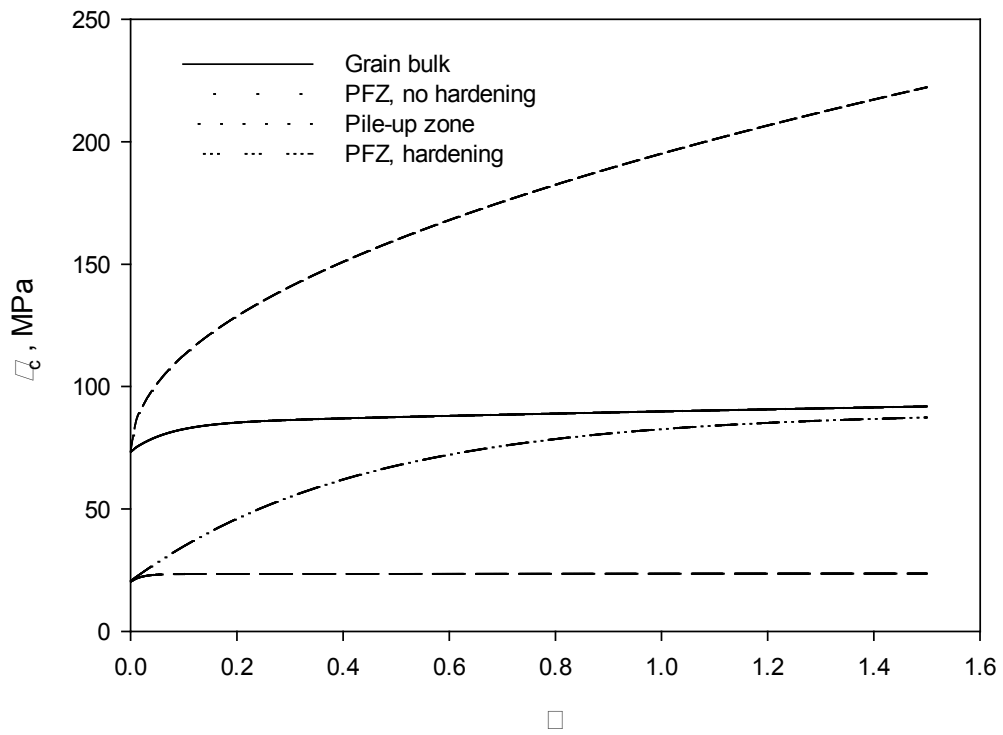
Figure 13: Evolution of slip resistance τ_c with accumulated slip Γ for different zones of the crystal.
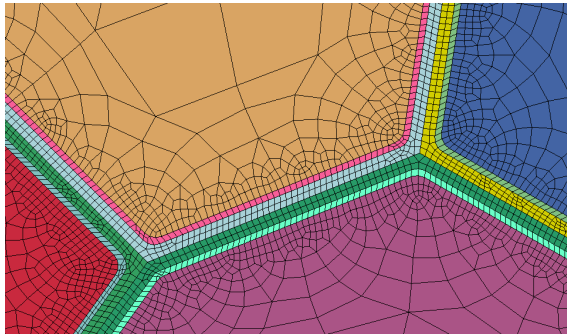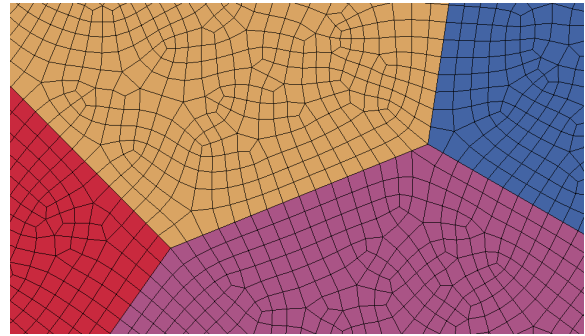
a)   b)

Figure 14: FEM mesh for the polycrystals with a) composite microstructure and b) grains without interfacial layers.
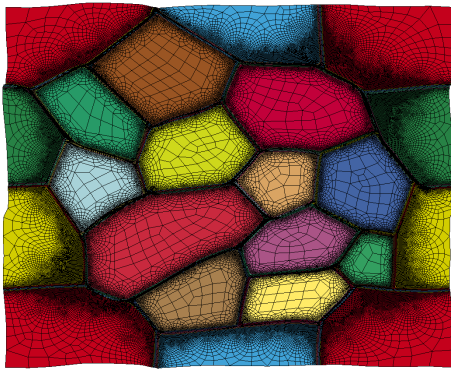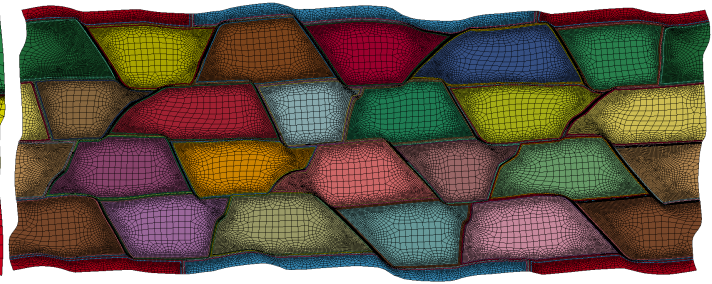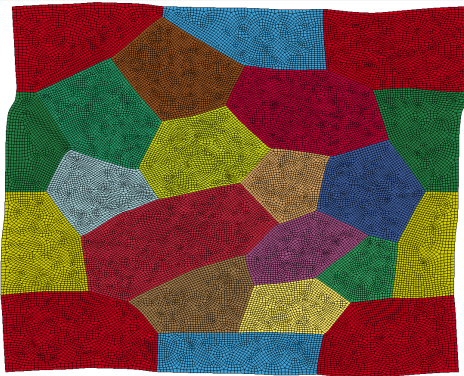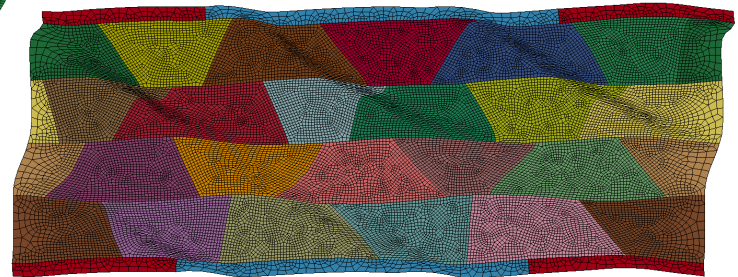
Figure 15: Deformed meshes of the composite (a,b) and homogeneous (c,d) models of the recrystallized (a,c) and fibrous (b,d) microstructure.
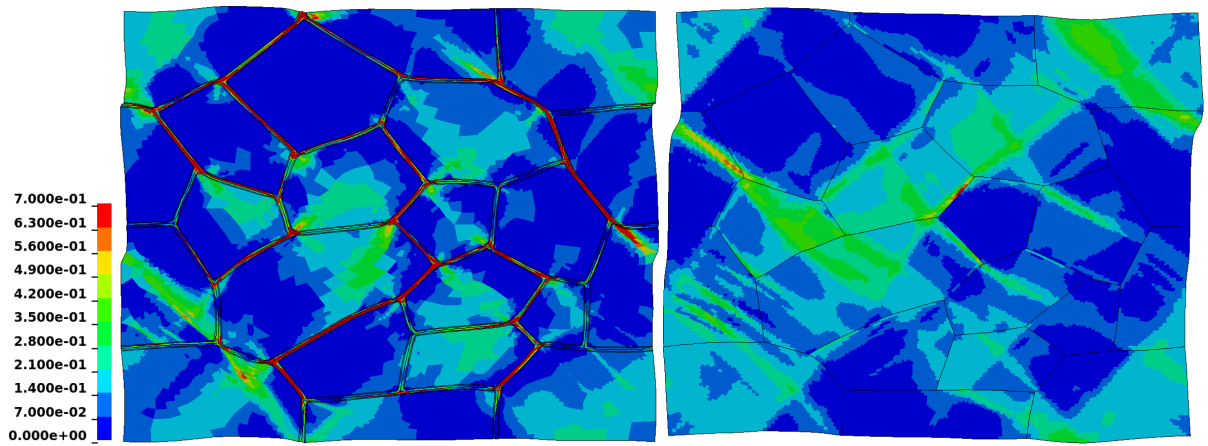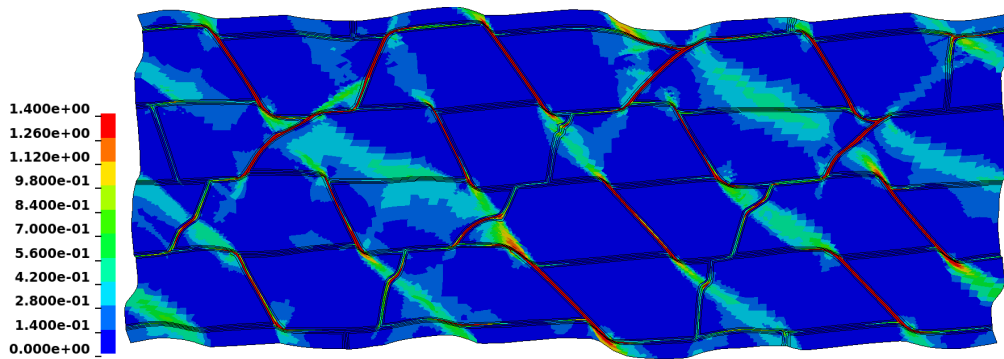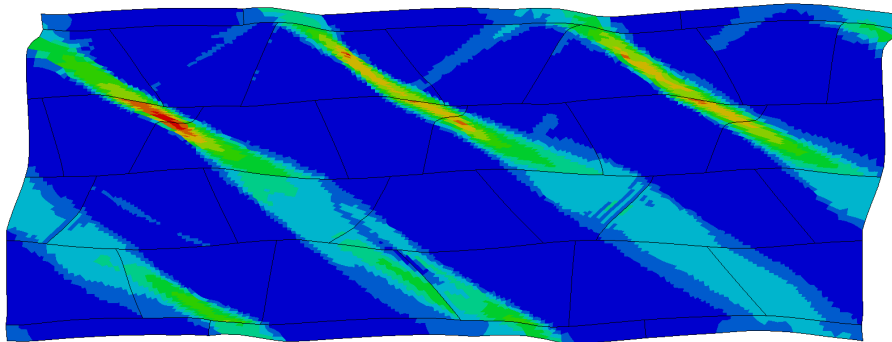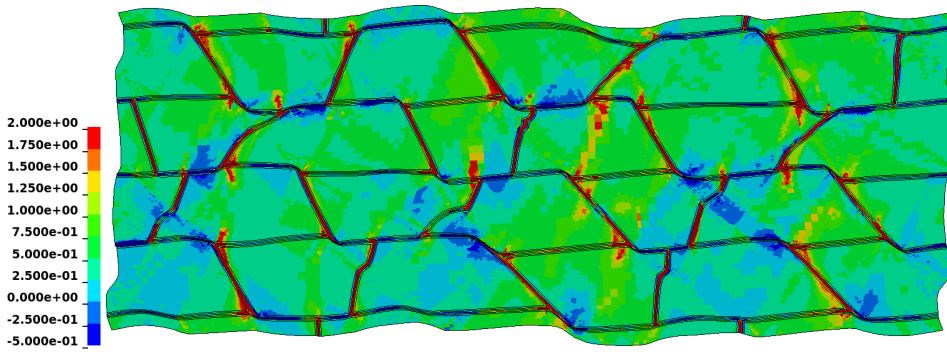
Figure 16: Contour plots of von Mises plastic strain distribution: a) composite and b) homogeneous models of the recrystallized microstructure; c) composite and d) homogeneous models of the fibrous microstructure.
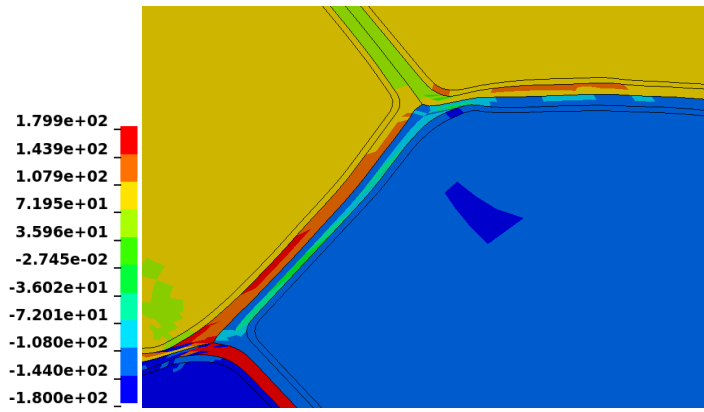
Figure 17: Contour plot of the first Euler angle φ_1 in degrees in a section of the recrystallized composite model.
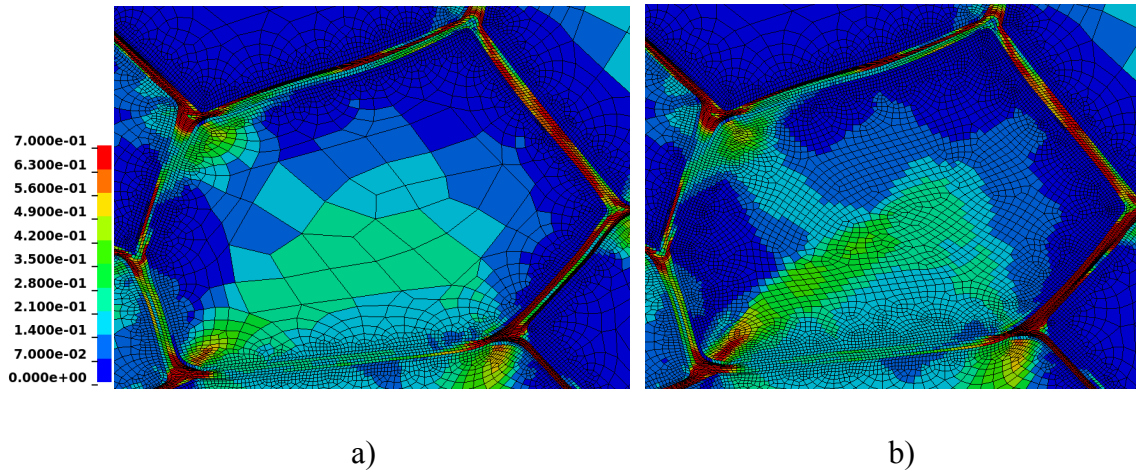
Figure 18: Contour plot of von Mises plastic strain in a part of the FEM model with a) the baseline mesh and b) a refined mesh.
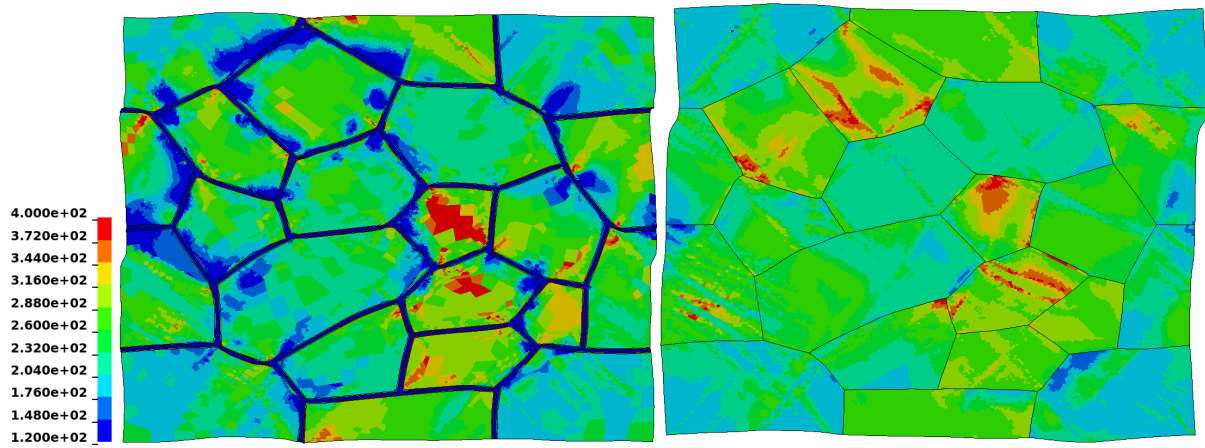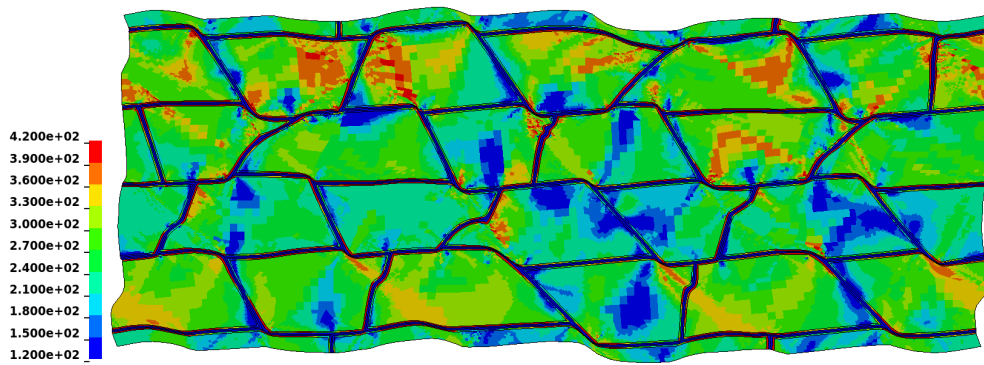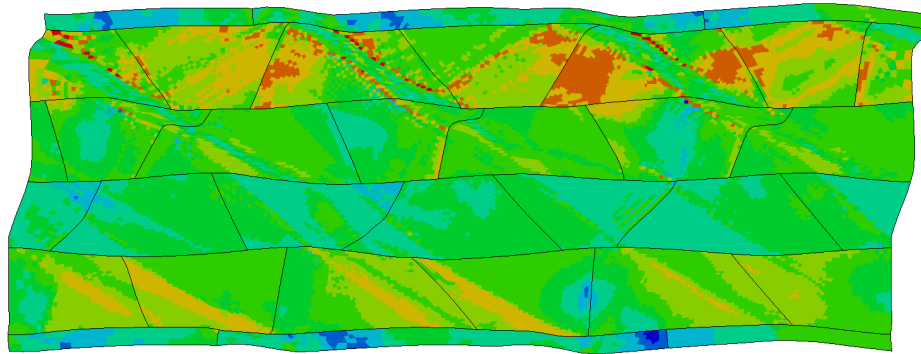
a)	b)
c)	
d)	

Figure 19: Contour plots of von Mises stress (MPa) distribution: a) composite and b) homogeneous models of the recrystallized microstructure; c) composite and d) homogeneous models of the fibrous microstructure.
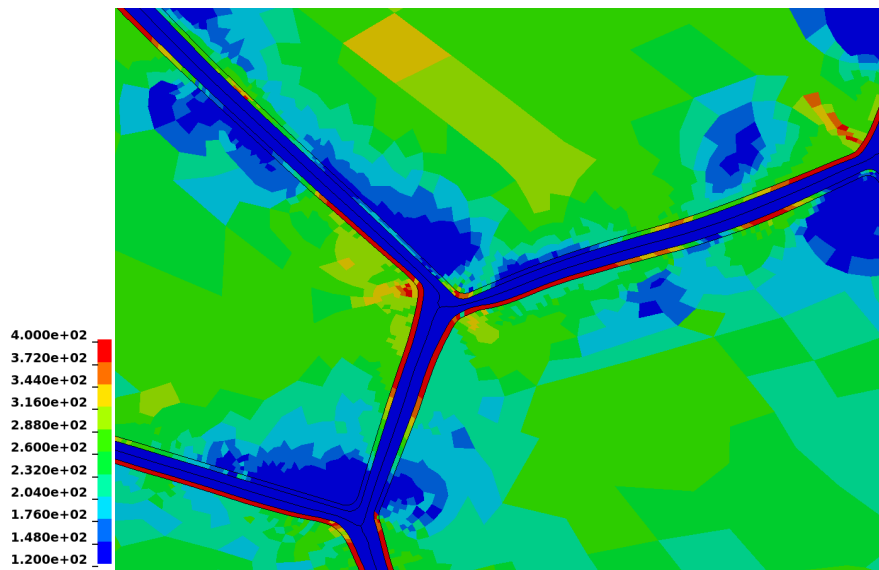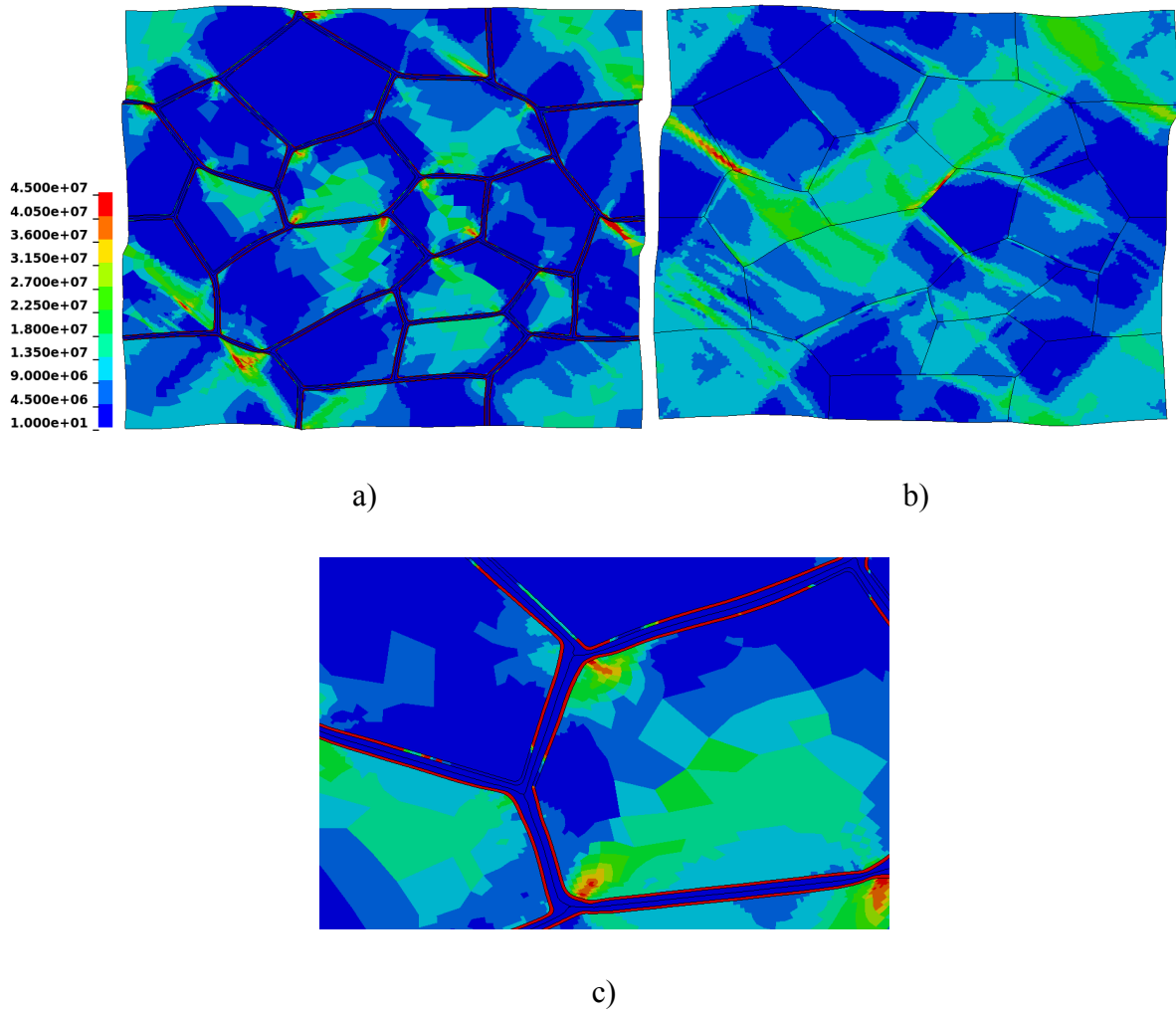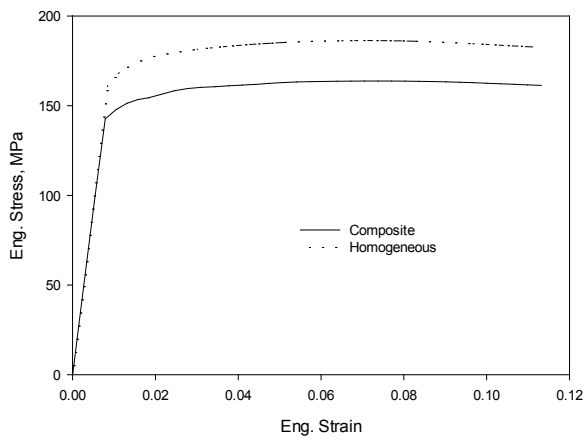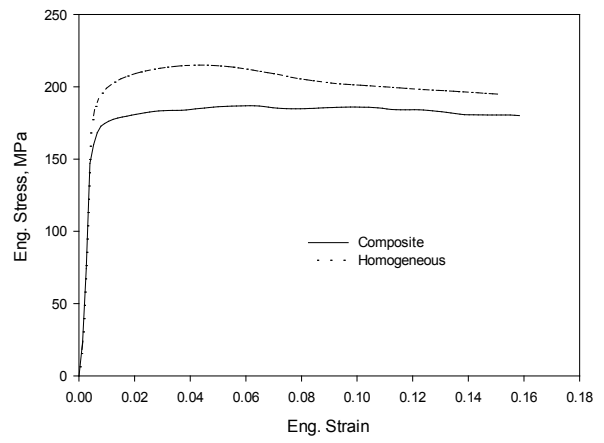
Figure 20: Contour plot of von Mises stress (MPa) distribution in a part of composite model of the recrystallized microstructure.
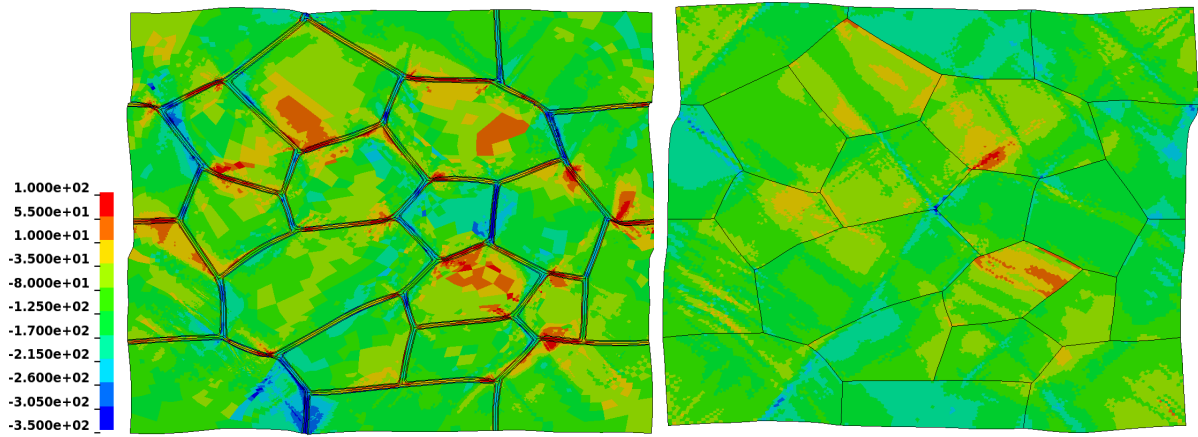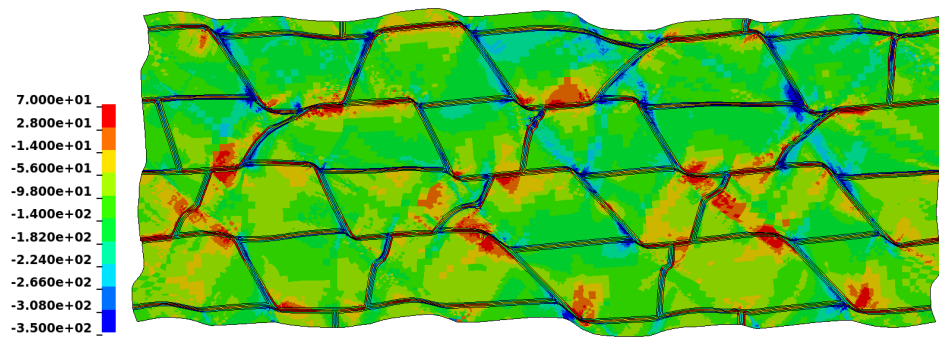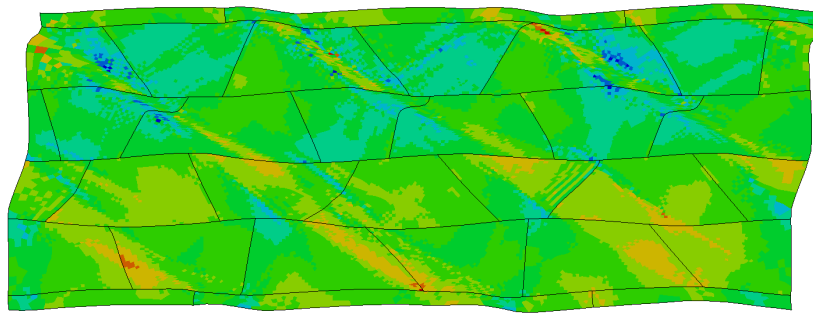
Figure 21: Contour plots of hydrostatic pressure (MPa) distribution: a) composite and b) homogeneous models of the recrystallized microstructure; c) composite and d) homogeneous models of the fibrous microstructure.
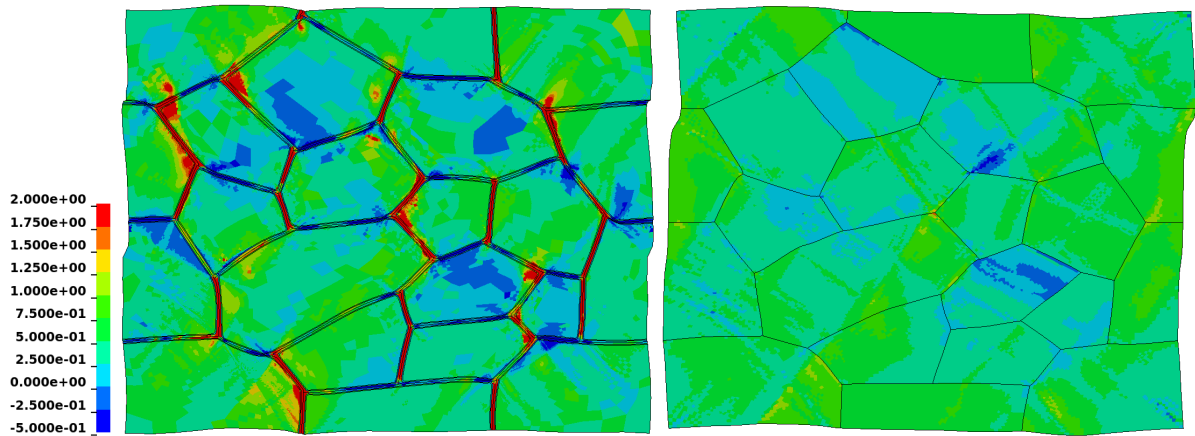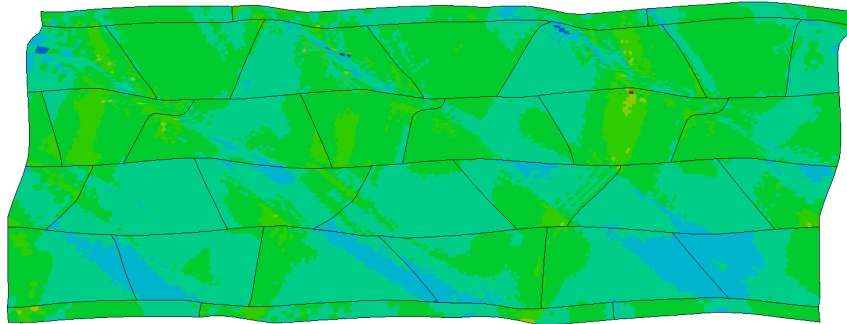
Figure 22: Contour plots of stress triaxiality distribution: a) composite and b) homogeneous models of the recrystallized microstructure; c) composite and d) homogeneous models of the fibrous microstructure.

Figure 23: Contour plots of dislocation density $\rho_{g1} + \rho_{g2}$ (mm^{-2}) in a) the composite model and b) the homogeneous model of the recrystallized microstructure, with a more detailed plot of a part of the composite model in c).

Figure 24: Engineering stress vs. strain curves for the composite and homogeneous model of a) recrystallized and b) fibrous microstructure.
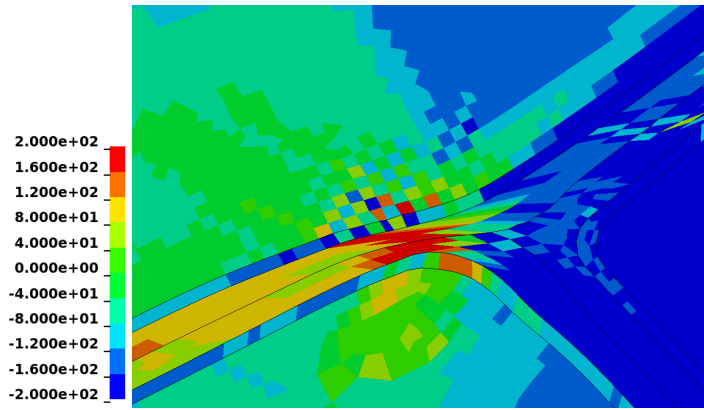
Figure 25: Checkerboard pattern in the contour plot of hydrostatic pressure for the recrystallized composite model.
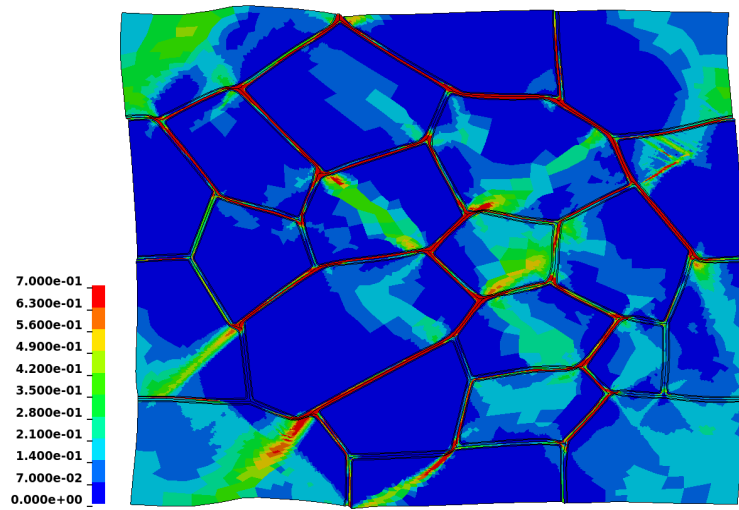
Figure 26: Contour plot of von Mises plastic strain in the composite model of the recrystallized microstructure with an alternative set of crystallographic orientations.
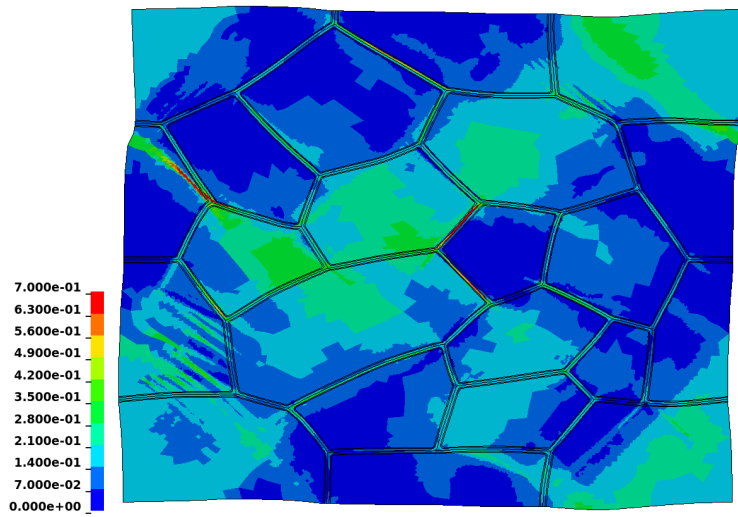
Figure 27: Contour plot of von Mises plastic strain in the composite model of the recrystallized microstructure with a work-hardening PFZ.

Tables

Table 1: Chemical composition of the AA6060 alloy (wt%)

Si	Mg	Fe	Mn	Cu	Zn	Ti
0.422	0.468	0.193	0.015	0.002	0.005	0.008

Table 2: Parameters of single crystal plasticity model

c_{11}, MPa	c_{12}, MPa	c_{44}, MPa	$\dot{\gamma}_0$, s^{-1}	m	$q_{\alpha\beta}$	μ, MPa	α	b, mm
106430	60350	28210	0.010	0.005	1.4, if $\alpha \neq \beta$ 1.0, if $\alpha = \beta$	24400	0.3	$2.86 \cdot 10^{-7}$

Table 3: Parameters of the single crystal plasticity model for different zones of the FEM mesh.

	τ_y, MPa	k_1, mm^{-1}	k_2	L_1, mm	L_2, mm	ρ_{g1}^{sat}, mm^{-2}
Grain interior	73.19	$1.51 \cdot 10^5$	27.23	$1.22 \cdot 10^{-2}$	—	$6.84 \cdot 10^7$
Pile-up zone	73.19	$1.51 \cdot 10^5$	27.23	$1.22 \cdot 10^{-2}$	$1.04 \cdot 10^{-3}$	$6.84 \cdot 10^7$
PFZ	20.50	$1.51 \cdot 10^5$	100.00	—	—	—